

Structural, electrical, and magnetic properties of nano Sr_{1-X}La_XFe₁₂O₁₉ (X = 0.2 - 0.8)

D. Baba Basha

N. Suresh Kumar

Chandra Babu Naidu K (✉ chandrababu954@gmail.com)

GITAM Deemed to Be University-Bangalore <https://orcid.org/0000-0002-0580-6383>

G. Ranjith Kumar

Research Article

Keywords: Nanoparticles, Structure, Electrical Properties, Magnetic Properties

Posted Date: March 11th, 2022

DOI: <https://doi.org/10.21203/rs.3.rs-1420921/v1>

License:  This work is licensed under a Creative Commons Attribution 4.0 International License.

[Read Full License](#)

Abstract

The current work mainly focused on the synthesis, structural, electrical, and magnetic characterization of $\text{Sr}_{1-x}\text{La}_x\text{Fe}_{12}\text{O}_{19}$ ($X = 0.2-0.8$) (SLFO) nanoparticles synthesized via the hydrothermal reaction technique. The hexagonal crystalline planes were determined using X-ray diffraction analysis. The obtained results indicated that the lattice constants were noted to be increasing from 0.58801 to 0.58825 nm ($a = b$), and 2.30309 to 2.30341 nm (c) with increase of 'X'. The morphological studies ensured that the grains as well as nanoparticles of SLFO acquired almost spherical shape. The optical properties were investigated using FTIR and UV-Visible spectra. The optical bandgap (E_g) of SLFO was found to be increasing from 1.866–2.118 eV with dopant content. The electrical properties of SLFO were studied in detail as a function of temperature, and frequency. In addition, the dielectric modulus, and impedance spectroscopy analysis was carried out to describe the space charge polarization, and electric conduction mechanism respectively. The hysteresis loop (M-H curves) of SLFO revealed the decrease of magnetization from 36.34–7.17 emu/g with 'X'.

1. Introduction

Among all the magnetic materials, the hexaferrites are the special class of materials with high coercivity. Thus, these materials are popularly known as hard magnetic materials. Therefore, the hexaferrites have got applications to manufacture permanent magnets. This kind of benefit is attributed to the parameters like high magnetization, magnetocrystalline anisotropy constant, inexpensive, thermal, and chemical stability [1]. Different properties such as crystal structure, particle size, surface morphology, preparation method, cation distribution etc., can reinforce to achieve the above-mentioned applications [1]. In general, the hexagonal ferrites are categorized into six types viz., M ($\text{SrFe}_{12}\text{O}_{19}$), W ($\text{BaZn}_2\text{Fe}_{16}\text{O}_{27}$), X ($\text{Ba}_2\text{Mg}_2\text{Fe}_{28}\text{O}_{46}$), Y ($\text{Ba}_2\text{Co}_2\text{Fe}_{12}\text{O}_{22}$), and Z ($\text{Ba}_3\text{Mn}_2\text{Fe}_{24}\text{O}_{41}$) [2]. The M-type hexaferrites come under hard ferrite category. The general chemical formula of M-type hexaferrite can be written as $\text{MFe}_{12}\text{O}_{19}$ (M = divalent elements like Ba, Sr, Pb, Zn, Mg, Ni etc.) which is like the magnetoplumbite structure [2].

Due to prominent electrical, magnetic, optical, and electromagnetic properties, M-type hexaferrites got applications in microwave absorbers, filters, diagnostics, ferrofluids, transformer cores, magnetic memories, magnetic recording, and high frequency devices [3]. Few of these applications were obtained from the M-type hexaferrite compounds such as $\text{BaFe}_{12}\text{O}_{19}$, $\text{SrFe}_{12}\text{O}_{19}$, and $\text{PbFe}_{12}\text{O}_{19}$ [4 - 23]. In addition, several scientists particularly focused on the synthesis and characterization of lanthanides (La, Sm, Gd, Nd, Pr etc) doped $\text{SrFe}_{12}\text{O}_{19}$ (SFO) in order to enhance the hardness of the SFO [3]. As a result, few properties were improved significantly. However, the reports on La-doped $\text{SrFe}_{12}\text{O}_{19}$ nanoparticles related to electrical, optical, magnetic properties were not available in the literature in detail. Therefore, we interested in preparing these samples in nanoform and studying their electrical and magnetic properties using the hydrothermal method.

2. Materials And Experimental Method

Hydrothermal synthesis technique is considered as one of the simplest and cost-effective technique to synthesize nanoparticles. With the help of hydrothermal technique, the $\text{Sr}_{1-x}\text{La}_x\text{Fe}_{12}\text{O}_{19}$ ($x = 0.0-0.8$) (SLFO) nanoparticles were prepared. In order to synthesize the SLFO nanoparticles, the precursor materials SrN_2O_6 , LaN_3O_9 , and FeN_3O_9 (which are of high pure in nature, and it is about 99.88 % from Sigma-Aldrich as mentioned in the flow chart (Figure.1)) were chosen as per the stoichiometric-ratio. Besides, the precursors were taken into glass beaker containing 50 ml of deionized water. In order to mix the precursors, the glass beaker was transferred on to the magnetic stirrer. The solution was stirred about 3 hours, at the time stirring the NaOH-solution was added drop by drop to acquire stable pH-value. Afterwards, the obtained aqueous solution was kept in a Teflon bowl of volume 300 mL which is enclosed in stainless-steel autoclave reactor. Later, the entire autoclave reactor was shifted into an oven for hydrothermal reaction for eight hours. Throughout the reaction the temperature of the oven was maintained at 150°C . After completing the reacton the oven was cooled down to room temperature naturally. Next, the obtained solution was cleaned several times by using distilled water and acetone to reduce the pH-value of the obtaied sample. This process was continued upto the sample pH reached to 7.

In the next step, the the sample was dried on the magnetic stirrer by maintaing the temperature of 60°C for two hours to remove the moisture present in the sample. Further, the obtained sample was ground until to get fine powder. Finally, the nanoparticles in powder form are subjected to different characterization such as X-Ray diffraction (XRD) (Bruker), TEM (Tecnai G20, FEI, USA), FESEM (Ultra 55, Carl Zeiss), FTIR (Shimadzu), UV-Visible spectrometer (JASCO, V-670 PC), LCR-controller (HIOKI 3532-50) and VSM (EV-7 H = ± 15000 Oe.) in order to disclose the phase, topography, functional-groups, band gap, hysteresis-behavior, and electrical properties respectively. The following figure 1 illustrates the schematic representation of synthesis procedure of as prepared nanoparticles.

3. Results And Discussion

3.1. X-ray diffraction (XRD) spectra

Fig. 2 represents the XRD-spectra SLFO nanoparticles which confirms the phase identification of prepared nanoparticles. These phases were indexed and compared with the standard JCPDS: 80-1198. From this, it was noted that all the diffraction phases were in consistent with the standard JCPDS. In addition, the highest counts were recorded for (114) reflection plane. The crystallite diameter at an average was calculated using Scherrer eq., $D_{\text{avg}} = 0.9\lambda_{\text{CuK}\alpha} / \beta \cos\theta$, $\lambda_{\text{CuK}\alpha}$ is the CuK α wavelength (0.15406 nm), β refers to full width half maxima (FWHM), and θ is associated to the diffraction angle [24]. The obtained D_{avg} values of $x = 0.2 - 0.6$ were found to be increasing from 4.5 – 14.8 nm. However, at $x = 0.8$, it was decreased to 5.2 nm. This can be usually attributed to the decreasing trend of microstrain (ϵ_s) (from 0.0282 -0.0210 radian) for $x = 0.2 - 0.6$ contents and increasing nature of the same to 0.0276 radian for $x = 0.8$ content. Similarly, the FWHM also followed the same trend as that of microstrain for all SLFO contents. This kind of behavior was earlier observed in the literature [25 - 29]. Besides, to provide a good agreement with these values, the microstrain ($\epsilon_{\text{W-H}}$), and average crystallite size ($D_{\text{W-H}}$) parameters were calculated by plotting Williamson-Hall (W-H) plots as depicted in Fig.3. These results were reported in

Table.1. The achieved data suggested that both the D_{W-H} and ϵ_{W-H} values were in good consistent with the same parameters attained using the Scherrer method [24].

Moreover, the lattice-parameters ($a=b\&c$) were calculated by utilizing the equation: $1/d^2=[1.333/a^2][h^2+hk+k^2+(l^2/c^2)]$ [25] and incorporated in Table.1. The obtained results indicated that the lattice-constants were noted to be enhancing from 0.58801 to 0.58825 nm ($a = b$), and 2.30309 to 2.30341 nm (c) with increase of 'X'. A detailed discussion can be given like this. Shannon ionic-radii table [30] exhibited that the ionic-radii of cations of SLFO are noted as $Sr^{+2} = 0.127$ nm, $La^{+3} = 0.122$ nm, $Fe^{+3} = 0.0645$ nm, and $Fe^{+2} = 0.080$ nm. This data ensured that the La^{+3} ions have lesser ionic radii than Sr^{+2} ions and greater than the ionic radii of ferric and ferrous ions. Therefore, La^{+3} cations have the reliable probability to occupy the Sr-site rather than the rest of the cationic sites. In the literature [31-35], it was observed that the incorporation of rare earth cations into the site of divalent element can induce the conversion of Fe^{+3} ions to Fe^{+2} ions within the hexaferrite system. Subsequently, in the current study, it is possible to replace the Sr^{+2} ions (high ionic radii) by La^{+3} ions (small ionic radii). However, one must observe a fact that the ionic radius of ferrous (Fe^{+2}) ion is larger than the ferric (Fe^{+3}) ion. To form SLFO compound, it was clear that a greater number of Fe^{+2} ions should be formed [32]. Hence, the enhancement of lattice-constants was identified as a function of dopant composition. This kind of nature was noticed in the case of bulk SLFO material reported by Seifert et al. [31, 32]. In some cases, the chemical composition, suppression effect of La^{+3} cations, and defects may also become accountable for present variation trend of unit-cell dimensions as well as unit cell volume (V_{cell}) [35]. The c/a ratio was found to be decreasing with 'X'. Furthermore, X-ray ($\rho_x = ZM.W/N_A V_{cell}$, where Z =effective-number of atoms per unit-cell, $M.W$ =molecular-weight, N_A =Avogadro's number, and V_{cell} =volume of the unit-cell) and bulk density (ρ_b is attained from Archimedes principle) [25] parameters were evaluated (see Table.1). The accomplished outcomes manifested that both the density parameters were noticed to be rising with increment of La-content in SFO system. This was ascribed to the rise of molecular-weight from approximately 1072 to 1102.8 g/mol. In addition, the porosity ($P = 1-(\rho_b/\rho_x)$) was calculated and detected to be declining from 18 to 8 %. This confirmed a fact that the pore content was reduced upon increasing the La-content. Finally, the specific surface area (S) established the decreasing trend from ~ 258 to 77 m^2/g (for $x = 0.2-0.6$). Beyond $X = 0.6$, the 'S' was about 217 m^2/g . This nature was attributed to the increasing trend of crystallite size up to $X = 0.6$ and decreasing manner beyond $X = 0.6$. Similar reports were noticed in the literature [25].

Table.1 Data on structural parameters of SLFO nanoparticles

X	0.2	0.4	0.6	0.8
D_{avg} (nm)	4.5	6.3	14.8	5.2
D_{W-H} (nm)	5.1	6.9	14.1	7.2
FWHM β_{avg} ($^{\circ}$)	2.584	2.556	1.816	2.542
ε_s (radian)	0.0282	0.0270	0.0210	0.0276
ε_{W-H} (radian)	0.0253	0.0201	0.0091	0.0237
a = b (nm)	0.58801	0.58810	0.58818	0.58825
c (nm)	2.30309	2.30317	2.30328	2.30341
c/a ratio	3.9168	3.9163	3.9159	3.9157
MW (g/mol)	1072.016	1082.272	1092.504	1102.784
V_{cell} (nm) ³	0.68960	0.68984	0.69006	0.69026
ρ_x (g/cm ³)	5.162	5.210	5.257	5.305
ρ_b (g/ cm ³)	4.233	4.428	4.679	4.881
P (%)	18	15	11	8
P_{avg} (nm)	16.2	35.2	44.1	37.2
G_{avg} (nm)	23.5	109.3	117.6	102.4
S (m ² /g)	258.3	182.9	77.1	217.5

3.2. Surface morphology

Fig.4 showed the FESEM photos of SLFO nanoparticles. In FESEM pictures, one can obviously notice that there were well-defined spherical shaped grains. Besides, these grains were distributed homogeneously. Comparatively, the X = 0.2 content acquired low apparent grain size while it seemed to be increasing from X = 0.2 – 0.6. But, for X=0.8, it was diminished. Later, with the help of linear intercept-method, the average grain-size (G_{avg}) was computed. In this technique, for each composition ten test-lines were drawn containing different test-lengths (L) at a specific working distance (WD) and magnification (M). Then, the total number of intersecting grains (N) was counted. Besides, all the parameter were inserted into the relation $G_{avg}=1.5L/MN$, where the symbols have their usual meaning. Thus, the experimental grain-size was accomplished, which was observed to be increased from 23.5 to 117.6 nm for X=0.2–0.6.

Furthermore, for X=0.8, it was observed to be reduced to 102.4nm. Similar kind of variation was noticed in average crystallite-size with the variation of 'X' in SLFO-nanoparticles.

The TEM pictures as shown in Fig.5 revealed the slightly distorted spheres like nanoparticles. Herein, the distribution of nanoparticles was seemed to be almost homogeneous. In addition, the average particle-size (P_{avg}) was computed and noticed to be upsurging from 16.2 to 44.1 nm for X=0.2–0.6 whereas the same was reduced to 37.2 nm for X=0.8. This manner was identical to the variation of D_{avg} and G_{avg} . Besides, the nanoparticles were appeared to be very close to each other. This can be normally attributed to various factors like magnetic interactions, agglomeration, size, charge etc [25].

3.3. Optical properties

The Fourier-transform infrared-spectra (FTIR) of SLFO-nanoparticles were shown in Fig.6. The FTIR-spectra evinced the formation of M-type hexagonal-structure. In which, the absorption bands located of about 550cm^{-1} were associated Sr-O & La-O (M-O) site whereas bands located of about 410cm^{-1} were related to Fe-O site of hexagonal-structure ($\text{MFe}_{12}\text{O}_{19}$). Hence, for the prepared SLFO samples the absorption bands noticed at ν_1' were associated to the M-site while ' ν_2' ' was associated to Fe-O bond. Therefore, this can expect that the development of hexagonal-structure of prepared samples. Furthermore, as observed in Fig.6, the formed additional-bands on either-side of iron-oxygen stretching vibrational site were ascribed to the presence of Fe^{+2} -ions. Generally, this may happen due to heat-treatment employed to the samples. Also, it was observed few band-sites at 1632.5 & 2109.5cm^{-1} and 3358.2 & 1338.6cm^{-1} . These sites were developed due to vibrational stretching which were appropriate for contortion of water molecules and O-H bonds [25-27].

Fig.7 expressed the diffuse reflectance spectra (DRS) of SLFO nanoparticles. It was seen that the maximum absorption wavelength (λ_{max}) was noted to be diminishing from 553.66 to 529.3 nm with respect to La-dopant content. Furthermore, $(\alpha hu)^n$ vs hu plots (where ' α ' is absorptivity, and ' hu ' is the photon energy) were drawn to obtain the optical energy band gap (E_g) of as prepared samples by considering $n=2$. Because, $n=2$ allows the direct-transition of charge-carriers between the energy-bands [25-27]. Therefore, as shown in Fig.8, we can write $(\alpha hu)^2$ versus hu instead of $(\alpha hu)^n$ versus hu . From, Fig.8 it is clear the value of E_g was progressively increased from 1.866 to 2.118eV with respect to dopant concentration. The value of E_g was obtained through extrapolation of linear portion of graph (Fig.8) towards the axis of photon-energy where absorptivity equal to zero [26]. Therefore, the outcomes are evinced that the increasing La-content causes the enhancement in the value of E_g .

3.4. Magnetic behavior

In case of SLFO nanoparticles, the magnetic nature is confirmed by means of hysteresis loops. These curves were plotted (see Fig.9) using the magnetization (M) versus magnetic-field (H) data. In general, one can expect that the magnetization should be decreased upon increasing the nonmagnetic La-composition. From Fig.9, it was evidently seen that, saturation magnetization was decreasing from 36.34

to 7.17 e.m.u./g (see Table.2) with increase of La-content. Thus, the expectations became true in this case. As discussed in the section.3.1 (XRD analysis), to replace the strontium site of large ionic radii by lanthanum of small ionic radii, there was an occurrence of conversion of ferric ions to ferrous ions. It was an established fact that Fe^{+3} ions contain the magnetic moment of $5\mu_B/\text{f.u.}$, while the Fe^{+2} -ions attain magnetic-moment of $4\mu_B/\text{f.u.}$ Indeed, this aspect implied a fact that the increasing La-content diminished the resultant magnetic moment thereby increasing the concentration of Fe^{+2} ions in SLFO. This manner was perceived in literature [31, 32] in case of bulk SLFO. Moreover, the increase of lattice constants with 'X' can be a second reason for this kind of behavior. That is, this can result in expansion of unit cell. Consequently, the magnetic exchange interactions will be decreased. This could be responsible for the reduction of magnetization thereby decreasing the magnetic moment of the spins. In addition, the high coercivity (H_c) of SLFO was estimated to be changing from 490-820 G with dopant. This can be an indication for the hard ferrite nature of SLFO. Besides, the retentivity (M_r) was found to be altering from 2.8 to 9.0 e.m.u./g. This suggested a fact that the variation of retentivity was unsystematic with 'X'.

Table.2 The magnetic and activation energy parameters of SLFO nanoparticles

X	0.2	0.4	0.6	0.8
M_s (e.m.u./g)	36.34	23.02	16.14	7.17
M_r (e.m.u./g)	6.3	9.0	5.6	2.8
H_c (G)	820	540	650	490
E_a (eV) for H-region	0.154	0.189	0.190	0.147
E_a (eV) for L-region	0.0376	0.0432	0.0443	0.0274

3.5. Temperature and frequency dependence of dielectric parameters

As a part of dielectric parameters, the dielectric constant (ϵ'), dielectric loss (ϵ''), ac-electrical-conductivity (σ_{ac}), and complex dielectric-modulus (M^*) were elucidated with respect to the variation of temperature (T) and frequency (f). It is a known fact that these parameters can mainly depend on distinct factor like sample preparation method, type of dopant, resultant compound, grain size, porosity, strain, density, and ionic radius [25]. Fig.10 depicted the ϵ' versus T plots. It was observed from the ϵ' -T plots (at $f = 1$ MHz) that the ϵ' of SLFO was remained constant until 400 K. It was accredited to weak and constant response of the charge-carriers at these temperatures. Beyond 400 K, there was a gradual increasing trend of dielectric constant for $X=0.2-0.6$. In contrast, $X=0.8$ revealed an abrupt increasing manner of dielectric constant without any intermediate dielectric relaxations. Meanwhile, $X=0.2-0.6$ contents exhibited dielectric relaxations between 533 – 583 K temperatures. On the whole, these dielectric relaxations were established owing to high thermal agitations among the electric dipoles. As a result, the entropy becomes

predominant at the relaxation temperatures which can in turn acquire the high magnitude of dielectric constant. Above 600 K, different compositions performed different Curie transition temperature (T_c) values. That is, the T_c values were diminished from 743 – 643 K with increase of 'X' from 0.2 – 0.8. This kind of trend was obtained due to reduction in exchange-interactions between two sites of SLFO thereby increasing the lattice constants with increase of dopant concentration. Likewise, ϵ'' versus T plots (Fig.11) stated almost similar T_c values as in case of dielectric constant versus temperature plots. Even, the variation-trend of ϵ'' - T plots was also identical to the ϵ' - T plots. Herein, the transitions were seemed to be saw tooth like nature.

The frequency variation of dielectric-constant and loss was described by means of ϵ' -f (Fig.12) and ϵ'' -f (Fig.13) plots respectively. In Fig.12, it was noticed that the dielectric constant of X=0.2–0.8 was decreasing from ~ 930 to ~ 30 at lower frequencies (between 100 Hz – 20 kHz). From this result, it was noticed that there was a maximum value of ϵ' at 100Hz while it was found to be 31 times smaller at 20 kHz. This kind of huge variation was earlier reported in Koop's double-layer theory [36]. This theory reported that the polycrystalline material is composed of two-layers which are (i) grain & (ii) grain-boundary. Indeed, these two layers are responsible for the higher and lower values of dielectric-constant at lower and higher frequencies. The analysis of Koop's theory suggested that the grain-boundaries are more resistive (low conductive) than the polycrystalline grains. Thus, at lower frequencies the charge carriers may not move and further they will be confined to certain microscopic region of the material. At this moment, the overcrowded nature of charge carriers usually takes place. This implied a fact that the all the charge carriers were not able to break the barrier (grain boundary layer) due to its high resistance. Therefore, the grain boundaries were predominant at the low frequencies and consequently it induced the huge amount of space charge or Maxwell-Wagner interfacial polarization. As a result, the maximum value of dielectric constant can be possible at low frequencies. This type of discussion was earlier reported by Wagner [37]. On the other hand, with increase of input field frequency, the electric dipoles become more active after absorbing sufficient energy from the input field. Hence, the charge carriers can break the grain boundary layer which subsequently reduces the resistance of barrier. This kind of approach of carriers will induce to obtain the high conductivity. At this moment, the grains (referred as low resistive or conductive segments) become more active. Therefore, the space charge polarization will be diminished to larger extent. This in turn leads to achieve low dielectric constant value at high frequencies. After 20 kHz, the dielectric constant of all samples was seemed to be obviously constant. However, the inset figure of Fig.12 showed that X = 0.6 content revealed the high ϵ' of ~ 18 at 1 MHz while the rest of the contents expressed moderate ϵ' values varying from $\sim 5 - 9$. In Fig.13, the ϵ'' -f plots indicated that there was an observation of huge ϵ'' value altering from 1830 – 34 between 100 Hz – 20 kHz. On the other hand, above $f = 20$ kHz, almost a constant variation of loss was observed. This trend was just identical to ϵ' behavior with 'f'. However, the inset figure of Fig.13 revealed a dielectric relaxation behavior at 3.5 for X = 0.2 – 0.8. Especially, X = 0.6 content performed the high loss of 10.28 at 3.5 MHz while X = 0.2, 0.4 & 0.8 contents showed the loss values from 1 – 4. The X = 0.6 content can be suitable for dielectric absorber applications at 1 – 5 MHz. Furthermore, this content may also work as microwave absorber at high frequencies.

Fig.14 indicated the behavior of σ_{ac} with temperature. It was clearly detected, that the conductivity was enhanced as a function of temperature. This was attributed to the thermal activation of charge carriers during the applied temperature range. Accordingly, hopping of electron takes place between ferric and ferrous ions. At very high temperatures, this electron hopping can appear to be predominant and therefore, the conductivity goes to larger extent. Herein, the values of T_c were noticed to be decreased from 743 to 643 K. Hence, one can expect the change of conduction-mechanism before and after transition-temperature. In view of this, the activation-energies were determined by drawing Arrhenius-plots (see Fig.14). In the plots, H-region corresponds to the high temperature region while L-region is associated to the low temperature region. In both the regions, the slopes were considered into account. Furthermore, with the help of a standard equation $E_a = 0.086$ (slope), the activation energies (E_a) were computed and depicted in Table.2. The obtained outcomes manifested that; the values of E_a in H-region were detected to be rising from 0.154 to 0.190 eV for X=0.2–0.6 contents. But for X=0.8 content, it was seemed to be diminished to 0.147 eV. In the same way, the activation energies of L-region were also decreased from 0.0376 to 0.0443 eV for X=0.2–0.6 compositions whereas, X=0.8 exhibited E_a of ~ 0.0274 eV. From the overall results, one can understand that the E_a values of H-region seemed to be larger than that of L-region. This kind of low E_a values were obtained owing to the limited availability of charge carriers caused by magnetic disordering [25]. However, the L-region was evolved owing to the electrical conduction process produced by the extrinsic charge carriers while H-region was formed because of polaron hopping [25]. Previously, it was reported that there must be a change of slope of gradient line on passing through the T_c [25]. In addition, the magnetic exchange interactions between the inner and outer electrons (e^-) on either side of T_c [25] were responsible for the different activation energies. In other way, the change of magnetic state from ferri to para at the T_c can reinforce for the occurrence of two different E_a values.

As depicted in Fig.15, the power-law fit was accomplished to $\log \sigma_{ac}$ - $\log \omega$ plots of X = 0.2 – 0.8 at various temperatures ranging from 313 – 813 K. Actually, the graphs from Fig.15 can afford dc-conductivity (σ_{dc}) and exponent (n) values. It was well-known fact that, σ_{ac} is a amalgamation of $\sigma_{dc}(T)$ (temperature-dependent) & $\sigma_{ac}(f)$ (frequency-dependent) terms. Mathematically, it can be written as follows: $\sigma_{ac}(f, T) = \sigma_{dc}(T) + \sigma_{ac}(f)$ [25]. Besides, all the temperatures the frequency-independent term in Fig. 15 can be identified from the invariant portion of the $\log \sigma_{ac}$ - $\log \omega$ plots. The computed σ_{dc} was found to be increasing from lower values to higher values as depicted in Table.4. That is, for X=0.2, 0.4, 0.6 & 0.8, the σ_{dc} was noticed to be almost increasing from 4.18E-07 - 2.54E-04, 1.72E-08 - 7.19E-05, 2.75E-08 - 6.51E-05 and 1.59E-08 - 1.95E-04 S/cm respectively. This established a fact that, low σ_{dc} was recorded for x=0.6 & 0.8 (large La-content). Moreover, exponent (n) values were also calculated and reported in Table.3. It was clear that, from the obtained 'n' values that it was decreasing from high value to low value for all the La-contents. This was in consistent with the reports made by Hiti [38]. As a whole, the 'n' value offers the ratio between back hop-rate and site-relaxation. Therefore, it can achieve a maximum-value of '1' & minimum-value of '0'. In current work, the value of 'n' was accomplished to be less than one only for all 'T'

values (313 – 813 K). This established a fact that site-relaxation happened in SLFO-nanoparticles was quicker than the hopping of polarons [25].

Table.3. DC-electrical conductivity & exponent parameters of SLFO nanoparticles

T (K)	0.2		0.4		0.6		0.8	
	σ_{dc} (S/cm)	n						
813	2.54E-04	0.415	7.19E-05	0.342	6.51E-05	0.368	1.95E-04	0.280
773	2.25E-04	0.434	5.86E-05	0.465	3.13E-05	0.386	5.62E-05	0.456
723	3.71E-05	0.462	2.72E-05	0.413	1.18E-04	0.458	1.67E-04	0.581
673	3.69E-05	0.578	1.94E-05	0.429	2.68E-05	0.653	7.05E-07	0.553
623	2.62E-05	0.616	1.40E-07	0.498	2.98E-05	0.609	2.41E-04	0.550
573	1.59E-05	0.645	4.12E-07	0.552	3.03E-06	0.679	4.19E-06	0.659
523	1.57E-05	0.639	1.49E-06	0.510	3.46E-06	0.735	3.87E-07	0.687
473	5.87E-06	0.689	4.35E-07	0.548	4.16E-07	0.720	4.25E-07	0.669
423	2.49E-06	0.779	1.22E-07	0.626	3.89E-07	0.789	2.44E-07	0.764
373	1.21E-07	0.716	3.91E-08	0.790	8.36E-09	0.852	1.75E-08	0.866
323	4.77E-07	0.780	2.39E-08	0.751	1.04E-07	0.823	6.68E-08	0.829
313	4.18E-07	0.852	1.72E-08	0.746	2.75E-08	0.841	1.59E-08	0.873

3.6. Dielectric and impedance spectroscopy analysis

The complex dielectric-modulus (M^*) is normally written as $M^*=M'+jM''$, where $M' = (\epsilon'/(\epsilon'^2 + \epsilon''^2))$ and $M'' = (\epsilon''/(\epsilon'^2 + \epsilon''^2))$. The electrical conduction as well as the space charge polarization effect can be well understood by means of studying the complex dielectric modulus formalism. The real and imaginary parts of dielectric modulus (M' & M'' respectively) were deliberated in case of SLFO nanoparticles. The related graphs were depicted in Fig.16 & 17. Fig.16 indicated that the real part of dielectric modulus versus input field frequency plots ($M' - f$) of X=0.2–0.8 showed relaxation (resonance) behaviour. Therefore, the complete plots were divided into couple of regions and the corresponding frequency was considered as relaxation frequency (f_r). These two regions were denoted as region-a ($< f_r$) and region-b ($> f_r$). The $M' - f$ plots of X=0.2–0.8 contents established a fact that the resonance frequencies were increased towards higher frequencies as a function of temperature from 313 – 813 K. It was practically seen that in case of X=0.2–0.8 compositions extended the f_r values $\geq \log f$ of 6.27, 6.16, 5.81, and 6.22 respectively. These f_r values were noted to be decreased from X = 0.2 – 0.6 and beyond that, it was

increased to $\log f = 6.22$ at room temperature. Usually, it was an established fact that the relaxation frequencies can be identified owing to the charge carrier accumulation at the interface of the grain-boundary. Thus, the space-charge polarization becomes predominant, and it can further show huge value of M' . In the same way, these kinds of relaxation were recorded in $M'' - f$ plots (see Fig.17) up to smaller extent. That means, the significant relaxations were seen at low temperatures (see $X = 0.4$ content) while small relaxations were observed at large temperatures. However, the space charge polarization mechanism was found in these materials. Herein, the low frequency relaxations specified a fact that the space-charges were triggered for small input field frequency of about $\log f = 5$ and further accumulated at the interface. Further, it was detected that the small M' -values were recorded at low f -values (<1 kHz). This was attributed to the electrode polarization effect. Moreover, the regions below $\log f = 6.27, 6.16, 5.81,$ and 6.22 (see M' - f plots) can be

dedicated to the region of long-range polarization. Inside this region, one can recognize the long-range hopping conduction-mechanism which was grown due to the long-range mobility of charge-carriers. Likewise, $M'' - f$ plots disclosed the small relaxations owing to long-distance moving ions. Conversely, high f_r -values were determined in case of M' - f & $M'' - f$ plots. These were formed owing to presence of ions confined to potential-well. This approach was found in the previous reports [25]. Moreover, the region beyond f_r was signified as short-range polarization-region where the short-range mobility of charge-carriers can be originated. Also, this can reflect the short-range hopping conduction-mechanism.

In order to discuss the behaviour of electrical conduction and relaxation the M' versus M'' plots were drawn and shown in Fig.18. In Fig.18, the semicircular arcs were associated to the contribution of grain & grain-boundaries in the electrical conduction-mechanism. Nevertheless, the noticed relaxations were partial in nature. Usually, these were developed due to partial relaxation-strength. Further, the presence of non-Debye relaxations in the prepared samples were confirmed from Fig.18 i.e., the centers in semicircles were existed below the M' -axis. Specifically, first semicircular-arc was connected to induced electrical-conduction owing to grain-contribution whereas the second-one was related to the contribution of grain-boundary in the conduction mechanism. Also, some distortions were noticed in M' versus M'' plots, which were evolved owing to intrinsic-factor such as micro-strain, pores, temperature, grain-size and moisture [25].

As we know that, the complex impedance (Z^*) parameter can provide the info about the behaviour of microstructure of polycrystalline-materials by this means elucidating the electrical-conduction mechanism of as prepared SLFO-nanoparticles. Actually, this induced the relation of $Z^*=Z'-jZ''$, where Z' & Z'' are real and imaginary-parts of complex impedance-parameter. Besides, Cole-Cole plots (Nyquist plots) were plotted as displayed in Fig.19. Nyquist plots were used to describe the conduction mechanism as function of rise of dopant (La) concentration in SLFO samples at all various temperatures between 313 to 813 K. Clearly, two semicircular arcs were found for $X=0.2-0.8$ contents. In particular, $X=0.2$ composition exhibited two semicircles clearly whereas remaining compositions showed slightly weak-arcs. The presence of partial relaxation-strength may be accountable for weak arcs [25]. Similarly, long travelling ions can induce partial arcs. In this, sample with $X=0.2$ content attained complete relaxation-strength

owing to existence of few-ions constraining to potential-well [25]. Though, the existence of semicircles specified the magnetic-semiconducting behaviour. In two arcs, the first arc designated the nature of grain whereas second one connected to grain-boundary. Normally, grain is large conductive-layer and its boundary acts as low conductive-layer. In current work, the Nyquist-plots were thoroughly examined via Z-view software (utilizing two RC-circuits). Accordingly, we accomplished the values of grain/grain-boundary resistance ($R_g(R_1)/R_{gb}(R_2)$) with their respective capacitances ($(C_g(C_1)/C_{gb}(C_2))$). The obtained values were tabulated in Table.4-7. This was evident that for all 'X' values, the values of grain-resistance and grain-boundary resistance were observed to be decreasing with increase of temperature (from 313 – 813 K). Consequently, the corresponding capacitance values (C_g & C_{gb}) were noticed to be increasing with temperature. Comparatively, the grain boundaries exhibit large resistance than the grains. With the help of intersecting portion of first and second arcs at Z'-axis the parameters of R_g and R_{gb} were elucidated. Therefore, first arc delivered R_g whereas second one established R_{gb} . This established a fact the grain boundaries consist few conductive layers while the grains constitute more conductive layers. Practically this was demonstrated from bulk-conductivity of grain ($\sigma_g=t/R_gA$, where 't'= thickness, and 'A'=area of cross section of pellet) and its boundary ($\sigma_{gb}=t/R_{gb}A$) (See Table.4 - 7). The obtained results confirmed that grains accomplished high electrical-conductivity than grain-boundaries. So, it was clear that current method satisfied the Koop's theory [36]. In addition, the electrical conductivity of X = 0.2 – 0.8 contents were found to be increasing with temperature and hence, it obeyed the Arrhenius law as mentioned in the previous work [25]. Apart from this, the induced relaxations were also deliberated. For this, we assumed the centers of arcs and noticed that if the centers of arcs were placed below real-axis. Therefore, it recommended that the non-Debye relaxations were mostly detected for x=0.2–0.8 [25]. In this view, the relaxation-time constants (τ) of grains (τ_g) and grain-boundaries (τ_{gb}) were computed. The obtained results (see Table.4 - 7) ensured that the time constant was increasing with increase of 'T'. Moreover, the second arcs expressed high ' τ_{gb} ' values.

Table.4 Impedance spectroscopy parameters of X = 0.2 content

T (K)	R _g (Ω)	R _{gb} (Ω)	C _g (F)	C _{gb} (F)	σ _g (S/cm)	σ _{gb} (S/cm)	τ _g (sec.)	τ _{gb} (sec.)
X = 0.2								
313	799444	2446922	8.01E-14	4.71E-12	8.83E-09	2.89E-09	6.40E-08	1.15E-05
333	774961	1995912	2.87E-13	6.37E-12	9.11E-09	3.54E-09	2.22E-07	1.27E-05
353	636436	1406376	4.36E-13	8.21E-12	1.11E-08	5.02E-09	2.77E-07	1.15E-05
373	444434	697000	6.48E-13	2.57E-11	1.59E-08	1.01E-08	2.88E-07	1.79E-05
393	173536	379385	9.23E-13	4.49E-11	4.07E-08	1.86E-08	1.60E-07	1.70E-05
413	148109	230729	9.88E-13	6.75E-11	4.77E-08	3.06E-08	1.46E-07	1.56E-05
433	62115	167080	2.94E-12	7.11E-11	1.14E-07	4.23E-08	1.83E-07	1.19E-05
453	53804	125336	3.15E-12	9.03E-11	1.31E-07	5.63E-08	1.69E-07	1.13E-05
473	49663	102425	3.75E-12	9.78E-11	1.42E-07	6.89E-08	1.86E-07	1.00E-05
493	41322	81456	4.62E-12	2.55E-10	1.71E-07	8.67E-08	1.91E-07	2.08E-05
513	35518	63156	5.11E-12	3.74E-10	1.99E-07	1.12E-07	1.81E-07	2.36E-05
533	27444	49580	6.64E-12	5.06E-10	2.57E-07	1.42E-07	1.82E-07	2.51E-05
553	21701	38004	7.32E-12	5.99E-10	3.25E-07	1.86E-07	1.59E-07	2.28E-05
573	17360	27571	8.05E-12	6.48E-10	4.07E-07	2.56E-07	1.40E-07	1.79E-05
593	12580	20888	9.68E-12	7.44E-10	5.61E-07	3.38E-07	1.22E-07	1.55E-05
613	9004	16082	1.56E-11	8.52E-10	7.84E-07	4.39E-07	1.40E-07	1.37E-05
633	6832	13662	3.12E-11	9.09E-10	1.03E-06	5.17E-07	2.13E-07	1.24E-05
653	4714	10479	4.72E-11	9.84E-10	1.5E-06	6.74E-07	2.23E-07	1.03E-05

673	2321	8150	5.35E-11	4.94E-09	3.04E-06	8.67E-07	1.24E-07	4.03E-05
693	1489	6220	6.25E-11	6.16E-09	4.74E-06	1.14E-06	9.31E-08	3.83E-05
713	1054	5011	7.15E-11	9.41E-09	6.7E-06	1.41E-06	7.54E-08	4.72E-05
733	836	3935	2.12E-10	3.68E-08	8.45E-06	1.79E-06	1.77E-07	1.45E-04
753	528	3177	9.36E-10	4.57E-08	1.34E-05	2.22E-06	4.94E-07	1.45E-04
773	317	2355	2.48E-09	5.82E-08	2.23E-05	3E-06	7.86E-07	1.37E-04
793	280	1774	4.42E-09	6.97E-08	2.52E-05	3.98E-06	1.24E-06	1.24E-04
813	195	1646	6.08E-09	8.60E-08	3.62E-05	4.29E-06	1.19E-06	1.42E-04

Table.5 Impedance spectroscopy parameters of X = 0.4 content

T (K)	R _g (Ω)	R _{gb} (Ω)	C _g (F)	C _{gb} (F)	σ _g (S/cm)	σ _{gb} (S/cm)	τ _g (sec.)	τ _{gb} (sec.)
X = 0.4								
313	4433887	4.9E+07	5.30E-14	2.58E-12	1.59E-09	1.44E-10	2.35E-07	1.26E-04
333	3841257	4.2E+07	8.97E-14	3.29E-12	1.84E-09	1.7E-10	3.45E-07	1.37E-04
353	3281653	3.4E+07	1.43E-13	4.07E-12	2.15E-09	2.08E-10	4.69E-07	1.38E-04
373	2977422	3.2E+07	3.33E-13	7.69E-12	2.37E-09	2.22E-10	9.91E-07	2.44E-04
393	2766950	2.9E+07	4.68E-13	2.49E-11	2.55E-09	2.4E-10	1.29E-06	7.32E-04
413	2588862	1.6E+07	4.99E-13	2.45E-11	2.73E-09	4.41E-10	1.29E-06	3.92E-04
433	2264920	7754721	9.26E-13	3.60E-11	3.12E-09	9.11E-10	2.10E-06	2.79E-04
453	1944513	3937347	9.96E-13	4.55E-11	3.63E-09	1.79E-09	1.94E-06	1.79E-04
473	753442	2059000	2.17E-12	3.91E-11	9.37E-09	3.43E-09	1.63E-06	8.05E-05
493	494478	1327717	1.54E-12	7.60E-11	1.43E-08	5.32E-09	7.61E-07	1.01E-04
513	308157	791443	2.75E-12	1.17E-10	2.29E-08	8.92E-09	8.47E-07	9.26E-05
533	236740	306541	3.40E-12	2.73E-10	2.98E-08	2.3E-08	8.05E-07	8.37E-05
553	150018	194131	3.69E-12	3.13E-10	4.71E-08	3.64E-08	5.54E-07	6.08E-05
573	92730	127932	4.00E-12	3.33E-10	7.62E-08	5.52E-08	3.71E-07	4.26E-05
593	71552	98808	4.70E-12	3.74E-10	9.87E-08	7.15E-08	3.36E-07	3.70E-05
613	73100	84360	7.65E-12	4.20E-10	9.66E-08	8.37E-08	5.59E-07	3.54E-05
633	60046	62790	9.03E-12	4.79E-10	1.18E-07	1.12E-07	5.42E-07	3.01E-05
653	40167	56235	2.58E-11	3.98E-10	1.76E-07	1.26E-07	1.04E-06	2.24E-05

673	18634	22902	2.85E-11	1.68E-09	3.79E-07	3.08E-07	5.31E-07	3.85E-05
693	10176	13084	3.24E-11	3.20E-09	6.94E-07	5.4E-07	3.30E-07	4.19E-05
713	6442	9950	3.62E-11	4.92E-09	1.1E-06	7.1E-07	2.33E-07	4.90E-05
733	4094	8152	5.77E-11	1.14E-08	1.72E-06	8.66E-07	2.36E-07	9.29E-05
753	2729	5631	4.56E-10	1.52E-08	2.59E-06	1.25E-06	1.24E-06	8.56E-05
773	1640	4543	7.30E-10	3.05E-08	4.31E-06	1.55E-06	1.20E-06	1.39E-04
793	1080	3258	2.46E-09	2.54E-08	6.54E-06	2.17E-06	2.66E-06	8.28E-05
813	203	2812	3.16E-09	3.24E-08	3.48E-05	2.51E-06	6.41E-07	9.11E-05

Table.6 Impedance spectroscopy parameters of X = 0.6 content

T (K)	R _g (Ω)	R _{gb} (Ω)	C _g (F)	C _{gb} (F)	σ _g (S/cm)	σ _{gb} (S/cm)	τ _g (sec.)	τ _{gb} (sec.)
X = 0.6								
313	2809385	2.7E+07	4.27E-14	2.93E-12	2.51E-09	2.59E-10	1.20E-07	8.00E-05
333	2571146	7.4E+07	8.75E-14	3.80E-13	2.75E-09	9.56E-11	2.25E-07	2.81E-05
353	2462010	7.5E+07	7.50E-14	2.76E-13	2.87E-09	9.43E-11	1.85E-07	2.07E-05
373	2336000	7E+07	1.86E-13	6.19E-12	3.02E-09	1.01E-10	4.34E-07	4.32E-04
393	2205940	5.6E+07	3.50E-13	2.82E-11	3.2E-09	1.26E-10	7.72E-07	1.59E-03
413	2008327	3.8E+07	3.88E-13	4.00E-11	3.52E-09	1.84E-10	7.79E-07	1.54E-03
433	1642555	9442031	4.10E-13	4.19E-11	4.3E-09	7.48E-10	6.73E-07	3.96E-04
453	989936	4826410	4.20E-13	5.34E-11	7.13E-09	1.46E-09	4.16E-07	2.58E-04
473	681423	974621	1.43E-12	5.79E-11	1.04E-08	7.25E-09	9.74E-07	5.64E-05
493	449065	638415	8.90E-13	9.08E-11	1.57E-08	1.11E-08	4.00E-07	5.80E-05
513	322459	444472	1.14E-12	2.43E-10	2.19E-08	1.59E-08	3.68E-07	1.08E-04
533	106224	195410	1.94E-12	2.12E-10	6.65E-08	3.61E-08	2.06E-07	4.14E-05
553	52809	72166	2.30E-12	3.60E-10	1.34E-07	9.79E-08	1.21E-07	2.60E-05
573	31140	55004	2.68E-12	3.86E-10	2.27E-07	1.28E-07	8.35E-08	2.12E-05
593	27468	49372	3.53E-12	3.36E-10	2.57E-07	1.43E-07	9.70E-08	1.66E-05
613	19662	32208	7.13E-12	4.92E-10	3.59E-07	2.19E-07	1.40E-07	1.58E-05
633	10061	16847	1.10E-12	5.64E-10	7.02E-07	4.19E-07	1.11E-08	9.50E-06
653	7328	11425	9.40E-12	5.87E-10	9.64E-07	6.18E-07	6.89E-08	6.71E-06

673	6618	9182	1.27E-11	3.05E-09	1.07E-06	7.69E-07	8.40E-08	2.80E-05
693	4299	8704	1.74E-11	2.69E-09	1.64E-06	8.11E-07	7.48E-08	2.34E-05
713	2049	6722	2.21E-11	5.80E-09	3.45E-06	1.05E-06	4.53E-08	3.90E-05
733	1688	5811	4.84E-11	2.40E-08	4.18E-06	1.22E-06	8.17E-08	1.39E-04
753	1007	4049	3.36E-10	1.86E-08	7.01E-06	1.74E-06	3.38E-07	7.53E-05
773	628	2965	6.72E-10	3.51E-08	1.12E-05	2.38E-06	4.22E-07	1.04E-04
793	377	2081	7.80E-10	4.11E-08	1.87E-05	3.39E-06	2.94E-07	8.55E-05
813	160	1832	1.65E-09	4.96E-08	4.41E-05	3.85E-06	2.64E-07	9.09E-05

Table.7 Impedance spectroscopy parameters of X = 0.8 content

T (K)	R _g (Ω)	R _{gb} (Ω)	C _g (F)	C _{gb} (F)	σ _g (S/cm)	σ _{gb} (S/cm)	τ _g (sec.)	τ _{gb} (sec.)
X = 0.8								
313	916647	3.6E+07	6.89E-14	2.53E-12	7.70E-09	1.94E-10	6.32E-08	9.23E-05
333	730846	3.4E+07	1.28E-13	3.66E-12	9.66E-09	2.09E-10	9.35E-08	1.24E-04
353	583249	2.2E+07	2.29E-13	4.92E-12	1.21E-08	3.27E-10	1.34E-07	1.06E-04
373	394307	1.4E+07	3.74E-13	1.07E-11	1.79E-08	5.09E-10	1.47E-07	1.49E-04
393	208432	8664420	5.89E-13	2.38E-11	3.39E-08	8.15E-10	1.23E-07	2.06E-04
413	123684	7946210	6.38E-13	3.92E-11	5.71E-08	8.89E-10	7.89E-08	3.11E-04
433	84267	5318240	3.20E-13	4.17E-11	8.38E-08	1.33E-09	2.70E-08	2.22E-04
453	62358	5006218	1.47E-12	5.68E-11	1.13E-07	1.41E-09	9.17E-08	2.84E-04
473	42367	3649201	1.88E-12	6.26E-11	1.67E-07	1.94E-09	7.96E-08	2.28E-04
493	29498	3000872	2.47E-12	2.40E-11	2.39E-07	2.35E-09	7.29E-08	7.20E-05
513	15360	2585484	2.80E-12	1.87E-10	4.6E-07	2.73E-09	4.30E-08	4.83E-04
533	12189	1509849	3.85E-12	2.77E-10	5.79E-07	4.68E-09	4.69E-08	4.18E-04
553	10364	724501	4.31E-12	3.40E-10	6.81E-07	9.75E-09	4.47E-08	2.46E-04
573	8476	583166	4.81E-12	3.74E-10	8.33E-07	1.21E-08	4.08E-08	2.18E-04
593	9410	302206	5.92E-12	4.39E-10	7.5E-07	2.34E-08	5.57E-08	1.33E-04
613	10868	188804	2.60E-12	5.13E-10	6.5E-07	3.74E-08	2.83E-08	9.69E-05
633	8087	72819	1.45E-11	6.06E-10	8.73E-07	9.7E-08	1.17E-07	4.41E-05
653	6410	56220	2.54E-11	6.37E-10	1.1E-06	1.26E-07	1.63E-07	3.58E-05

673	5503	38462	2.97E-11	2.69E-09	1.28E-06	1.84E-07	1.63E-07	1.03E-04
693	3038	10999	3.58E-11	3.52E-09	2.32E-06	6.42E-07	1.09E-07	3.87E-05
713	1118	7544	4.19E-11	6.28E-09	6.32E-06	9.36E-07	4.68E-08	4.74E-05
733	628	5008	7.64E-11	1.83E-08	1.12E-05	1.41E-06	4.80E-08	9.16E-05
753	447	4892	5.70E-10	2.43E-08	1.58E-05	1.44E-06	2.55E-07	1.19E-04
773	308	3529	1.01E-09	3.29E-08	2.29E-05	2E-06	3.11E-07	1.16E-04
793	364	2758	2.33E-09	4.07E-08	1.94E-05	2.56E-06	8.48E-07	1.12E-04
813	149	2420	3.46E-09	5.18E-08	4.74E-05	2.92E-06	5.16E-07	1.25E-04

4. Conclusions

In this study, the SLFO nanoparticles were prepared using the hydrothermal method. The La-content in the SLFO system was varied from $X = 0.2 - 0.8$. The diffraction pattern evidenced the hexagonal crystal structure. In addition, the lattice constants were observed to be increasing from 0.58801 to 0.58825 nm ($a = b$), and 2.30309 to 2.30341 nm (c) with increase of 'X'. The FESEM and TEM pictures indicated the spheres like grains as well as particles in the morphology. Furthermore, the E_g values were identified to be increasing from 1.866 to 2.118 eV upon increasing 'X'. The M-H loops of SLFO revealed the decreasing trend of magnetization from 36.34 - 7.17 emu/g with 'X'. The $X = 0.6$ content revealed high dielectric constant (~ 18) and high dielectric loss (10.85) at high frequencies. Therefore, this composition can be suitable for dielectric absorber applications at 1 – 5 MHz. The E_a values of H-region were altered from 0.147 to 0.190 eV while the L-region showed the same changing from 0.0274 to 0.0443 eV. Using the power law fit, the dc-conductivity and exponents were computed. The dielectric modulus formalism provided the clear evidence for the space charge polarization mechanism. Besides, the short range and long-range hopping conduction mechanism was described. The Cole-Cole plots were used to elucidate the contribution of grain and grain boundary in the electrical conduction mechanism. The obtained results indicated that the grains accomplished more electrical-conductivity than the grain-boundaries.

Declarations

Acknowledgements

The author would like to thank Deanship of Scientific Research at Majmaah University for supporting this work under Project Number No.....

Conflict of interest: The authors declare that they have no conflicts of interest.

References

1. B. Grindi, Z. Beji, G. Viau, A. BenAli, Microwave-assisted synthesis and magnetic properties of M-SrFe₁₂O₁₉ nanoparticles, *Journal of Magnetism and Magnetic Materials* 449 (2018) 119-126.
2. Modification of the Magnetic Properties of Co₂Y Hexaferrites by Divalent and Trivalent Metal Substitutions, *Solid State Phenomena* 241 (2016) 93-125
3. Nazia Yasmin, Muhammad Zubair Iqbal, Maria Zahid, Saher Fatima Gillani, Muhammad Naeem Ashiq, Iqra Inam, Sidra Abdulsatar, Muhammad Safdar, Misbah Mirz, Structural and magnetic studies of Ce-Zn doped M-type SrFe₁₂O₁₉ hexagonal ferrite synthesized by sol-gel auto-combustion method, *Ceramics International* 45 (2019) 462-467
4. Ahmed, M. A., Helmy, N., & El-Dek, S. I., Innovative methodology for the synthesis of Ba-M hexaferrite BaFe₁₂O₁₉ nanoparticles, *Materials Research Bulletin* 48 (2013) 3394–3398.
5. Huang, B., Li, C., & Wang, J., Template synthesis and magnetic properties of highly aligned barium hexaferrite (BaFe₁₂O₁₉) nanofibers, *Journal of Magnetism and Magnetic Materials* 335 (2013) 28–31.
6. Li, Y., Wang, Q., & Yang, H., Synthesis, characterization and magnetic properties on nanocrystalline BaFe₁₂O₁₉ ferrite, *Current Applied Physics* 9 (2009) 1375–1380.
7. Kaynar, M. B., Özcan, Ş., & Shah, S. I., Synthesis and magnetic properties of nanocrystalline BaFe₁₂O₁₉, *Ceramics International* 41 (2015) 11257–11263.
8. Li, C.-J., Huang, B.-N., & Wang, J.-N., Effect of aluminum substitution on microstructure and magnetic properties of electrospun BaFe₁₂O₁₉ nanofibers, *Journal of Materials Science* 48 (2012) 1702–1710.
9. Mattei, J.-L., Le, C. N., Chevalier, A., Maalouf, A., Noutehou, N., Queffelec, P., & Laur, V., A simple process to obtain anisotropic self-biased magnets constituted of stacked barium ferrite single domain particles, *Journal of Magnetism and Magnetic Materials*, 451 (2018) 208–213.
10. Mosleh, Z., Kameli, P., Ranjbar, M., & Salamati, H., Effect of annealing temperature on structural and magnetic properties of BaFe₁₂O₁₉ hexaferrite nanoparticles, *Ceramics International* 40 (2014) 7279–7284.
11. Shen, X., Liu, M., Song, F., & Meng, X., Structural evolution and magnetic properties of SrFe₁₂O₁₉ nanofibers by electrospinning, *Journal of Sol-Gel Science and Technology*, 53 (2009) 448–453.
12. Martirosyan, K. S., Galstyan, E., Hossain, S. M., Wang, Y.-J., & Litvinov, D., Barium hexaferrite nanoparticles: Synthesis and magnetic properties, *Materials Science and Engineering: B* 176 (2011) 8–13.

13. Castro, W. S., Corrêa, R. R., Paulim Filho, P. I., Rivas Mercury, J. M., & Cabral, A. A., Dielectric and magnetic characterization of barium hexaferrite ceramics, *Ceramics International*, 41 (2015) 241–246.
14. Hou, C., Liu, G., Dang, F., Zhang, Z., & Chen, J., Effect of strontium substitution on microstructure and magnetic properties of electrospinning BaFe₁₂O₁₉ nanofibers, *Journal of Wuhan University of Technology-Mater. Sci. Ed.*, 32 (2017) 871–874.
15. Liu, Y., Drew, M. G. B., & Liu, Y., Optimizing the methods of synthesis for barium hexagonal ferrite-An experimental and theoretical study, *Materials Chemistry and Physics*, 134 (2012) 266–272.
16. Song, F., Shen, X., Xiang, J., & Song, H., Formation and magnetic properties of M-Sr ferrite hollow fibers via organic gel-precursor transformation process, *Materials Chemistry and Physics*, 120 (2010) 213–216.
17. S. Diaz - Castanon, F. Leccabue, B.E. Watts, R. Yapp, PbFe₁₂O₁₉ thin films prepared by pulsed laser deposition on Si/SiO₂ substrates, *Journal of Magnetism and Magnetic Materials* 220 (2000) 79-84
18. A. Haq, M. Anis-ur-Rehman, Effect of Pb on structural and magnetic properties of Ba-Hexaferrite, *Physica B* 407 (2012) 822–826.
19. S. Diaz-Castanon, J. L. Sanchez LI, E. Estevez-Rams, F. Leccabue, B.E. Watts, Magneto-structural properties of PbFe₁₂O₁₉ hexaferrite powders prepared by decomposition of hydroxide-carbonate and metal-organic precipitates, *Journal of Magnetism and Magnetic Materials* 185 (1998) 194-198
20. S. Diaz-Castanon, J. C. Faloh-Gandarilla, F. Leccabuec, G. Albanese, The optimum synthesis of high coercivity Pb-M hexaferrite powders using modifications to the traditional ceramic route, *Journal of Magnetism and Magnetic Materials* 272–276 (2004) 2221–2223
21. Nan Yang, Haibin Yang, JunjiJia, Xiaofen Pang, Formation and magnetic properties of nanosized PbFe₁₂O₁₉ particles synthesized by citrate precursor technique, *Journal of Alloys and Compounds* 438 (2007) 263-267
22. Guo-Long Tan and Wei Li, Ferro-electricity and Ferromagnetism of M-type Lead Hexaferrites, *Journal of American Ceramic Society* 98 (2015) 1812-1817
23. Guo-Long Tan. Min Wang, Multiferroic PbFe₁₂O₁₉, *Journal of Electro Ceramics* 26 (2011) 170-174
24. Scherrer, P. Bestimmung der Grosse und der Inneren Struktur von Kolloidteilchen Mittels Rontgenstrahlen, *Nachrichten von der Gesellschaft der Wissenschaften, Gottingen. Mathematisch-Physikalische Klasse*, 2 (1918) 98-100
25. N. Raghuram, T. S. Rao, K. Chandra Babu Naidu, Investigations on Functional Properties of Hydrothermally Synthesized Ba_{1-x}Sr_xFe₁₂O₁₉ (x = 0.0 - 0.8) Nanoparticles, *Material Science in Semiconductor Processing* 94 (2019) 136-150
26. U. Naresh, R. J. Kumar, K. Chandra Babu Naidu, Optical, Magnetic and Ferroelectric Properties of Ba_{0.2}Cu_{0.8-x}La_xFe₂O₄ (x = 0.2 - 0.6) Nanoparticles, *Ceramics International* 45 (2019) 7515-7523
27. Mohammad Tasleem, Mohd. Hashim, K. Chandra Babu Naidu , Syed Asad Ali, D. Ravinder, Optical and Electronic Properties of Copper & Cobalt Substituted Nano SrBaFe₁₂O₁₉ Synthesized by Sol-Gel

- Autocombustion Method, Applied Physics A, (2019) 125:305, DOI: 10.1007/s00339-019-2618-5
28. N. S. Kumar, R. P. Suvarna, K. Chandra Babu Naidu, Microwave Heated Lead Cobalt Titanate Nanoparticles Synthesized by Sol-Gel Technique: Structural, Morphological, Dielectric, Impedance and Ferroelectric Properties, Materials Science and Engineering B 242 (2019) 23-30
 29. N. Boda, G. Boda, K. Chandra Babu Naidu, M. Srinivas, K. M. Batoo, D. Ravinder, A.P. Reddy, Effect of Rare Earth Elements on Low Temperature Magnetic Properties of Ni and Co-Ferrite Nanoparticles, Journal of Magnetism and Magnetic Materials, 473 (2019) 228-235
 30. R.D. Shannon Revised Effective Ionic Radii and Systematic Studies of Interatomic Distances in Halides and Chalcogenides, *Acta Cryst.* **A 32** (1976) 751-767.
 31. D. Seifert, J. Topfer, F. Langenhorst, J.M. Le Breton, H. Chiron, L. Lechevallier, Synthesis and magnetic properties of La-substituted M-type Sr hexaferrites, Journal of Magnetism and Magnetic Materials 321 (2009) 4045 - 4051
 32. Daniela Seifert, Jorg Topfer, Markus Stadelbauer, Roland Grossinger, and Jean-Marie Le Breton, Rare-Earth-Substituted $Sr_{1-x}Ln_xFe_{12}O_{19}$ Hexagonal Ferrites, J. Am. Ceram. Soc., 94 (2011) 2109 – 2118
 33. Long Peng, Lezhong Li, Rui Wang, Yun Hu, Xiaoqiang Tu, Xiaoxi Zhong, Effect of La-CO substitution on the crystal structure and magnetic properties of low temperature sintered $Sr_{1-x}La_xFe_{12-x}Co_xO_{19}$ ($x = 0 - 0.5$) ferrites, Journal of Magnetism and Magnetic Materials 393 (2015) 399 – 403
 34. Muhammad Aslam Malana, Raheela Beenish Qureshi, Muhammad Naeem Ashiq, Muhammad Fahad Ehsan, Synthesis, structural, magnetic and dielectric characterizations of molybdenum doped calcium strontium M-type hexaferrites, Ceramics International 42 (2016) 2686 – 2692
 35. Ankush Thakur, R.R. Singh, P.B. Barman, Synthesis and characterizations of Nd^{3+} doped $SrFe_{12}O_{19}$ Nanoparticles, Materials Chemistry and Physics 141 (2013) 562 - 569
 36. C. G. Koops, On the Dispersion of Resistivity and Dielectric Constant of Some Semiconductors at Audio frequencies, Physical Review 83 (1951) 121-124
 37. K.W. Wagner, The Distribution of Relaxation Times in Typical Dielectrics, Ann. Phys., 40 (1913) 817
 38. M A Ell Hiti, AC. electrical conductivity of Ni–Mg ferrites, J. Phys. D: Appl. Phys. 29 (1996) 501–505.

Figures

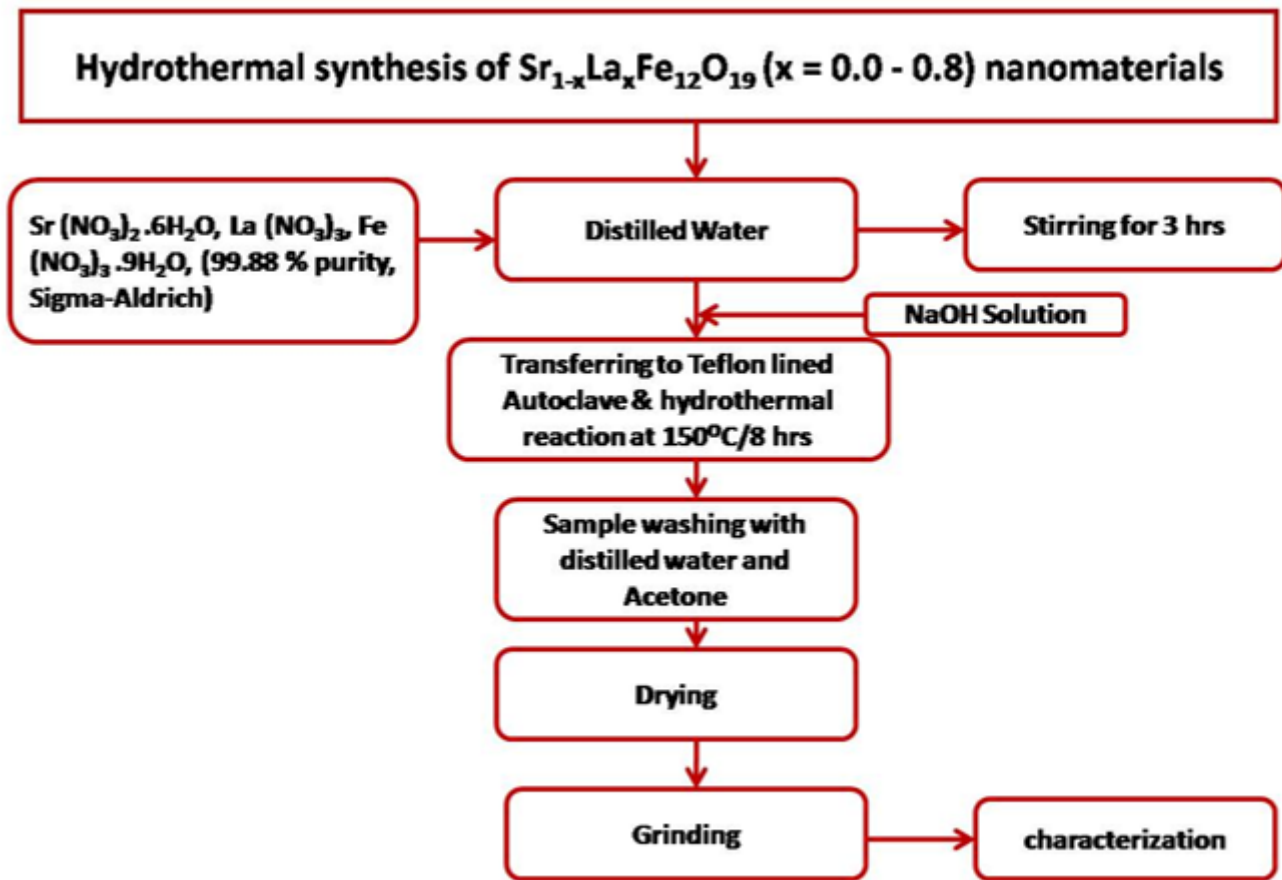


Figure 1

Schematic representation of synthesis of SLFO nanoparticles

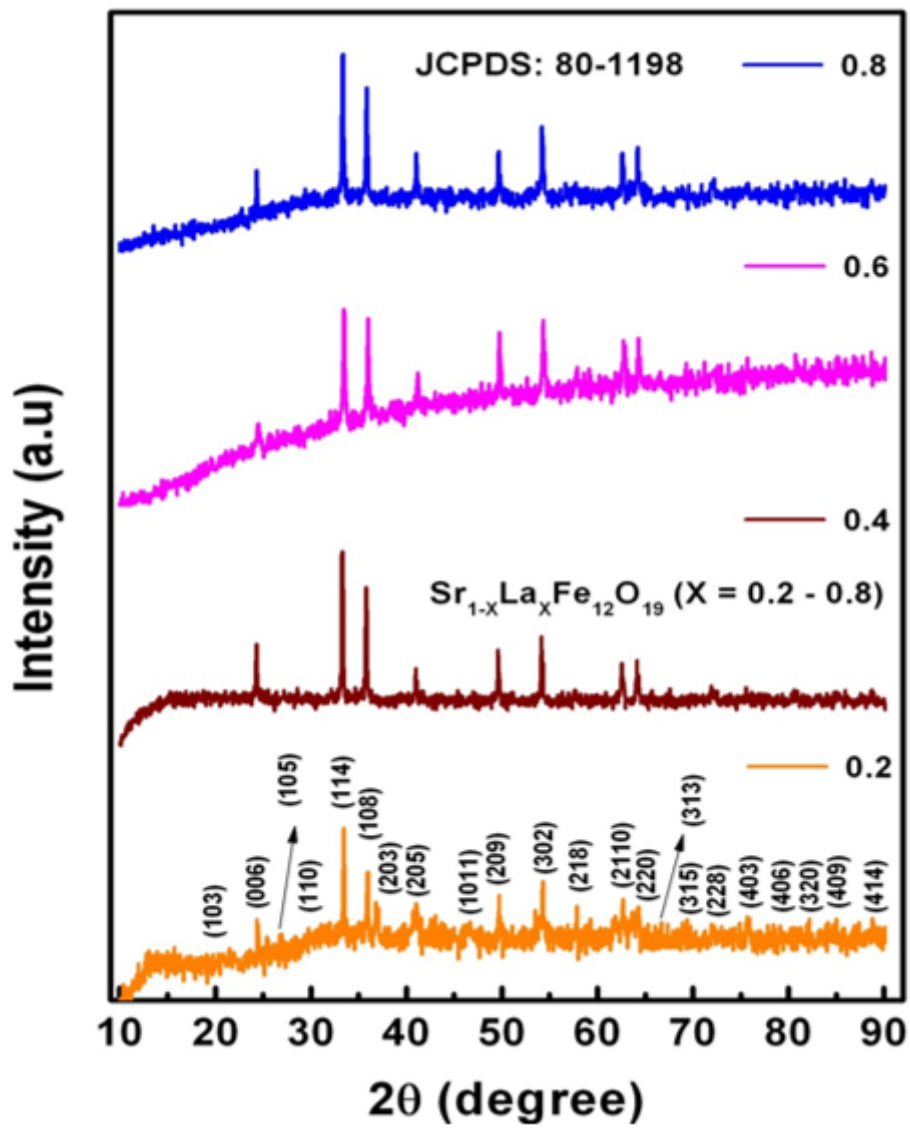


Figure 2

XRD spectra of SLFO nanoparticles

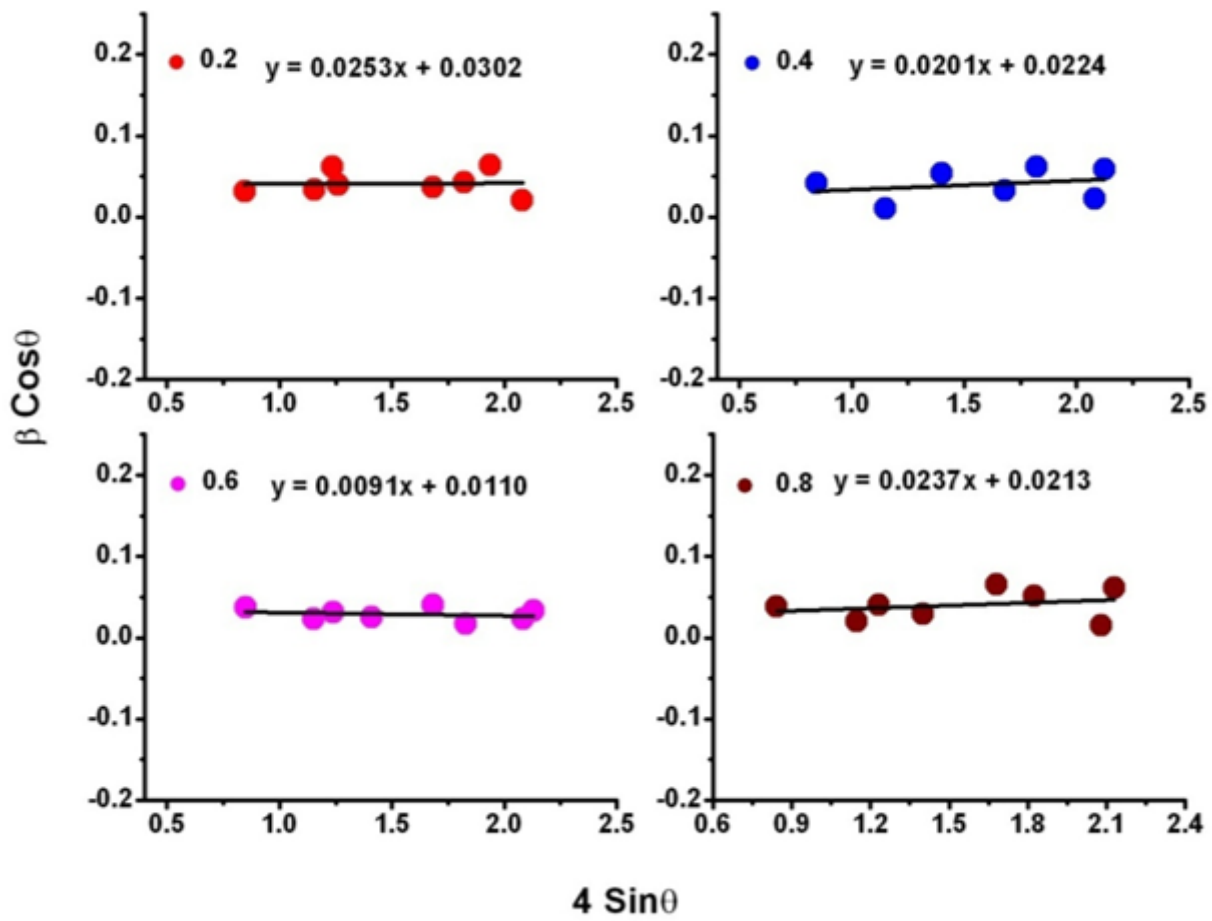


Figure 3

W-H plots of SLFO nanoparticles

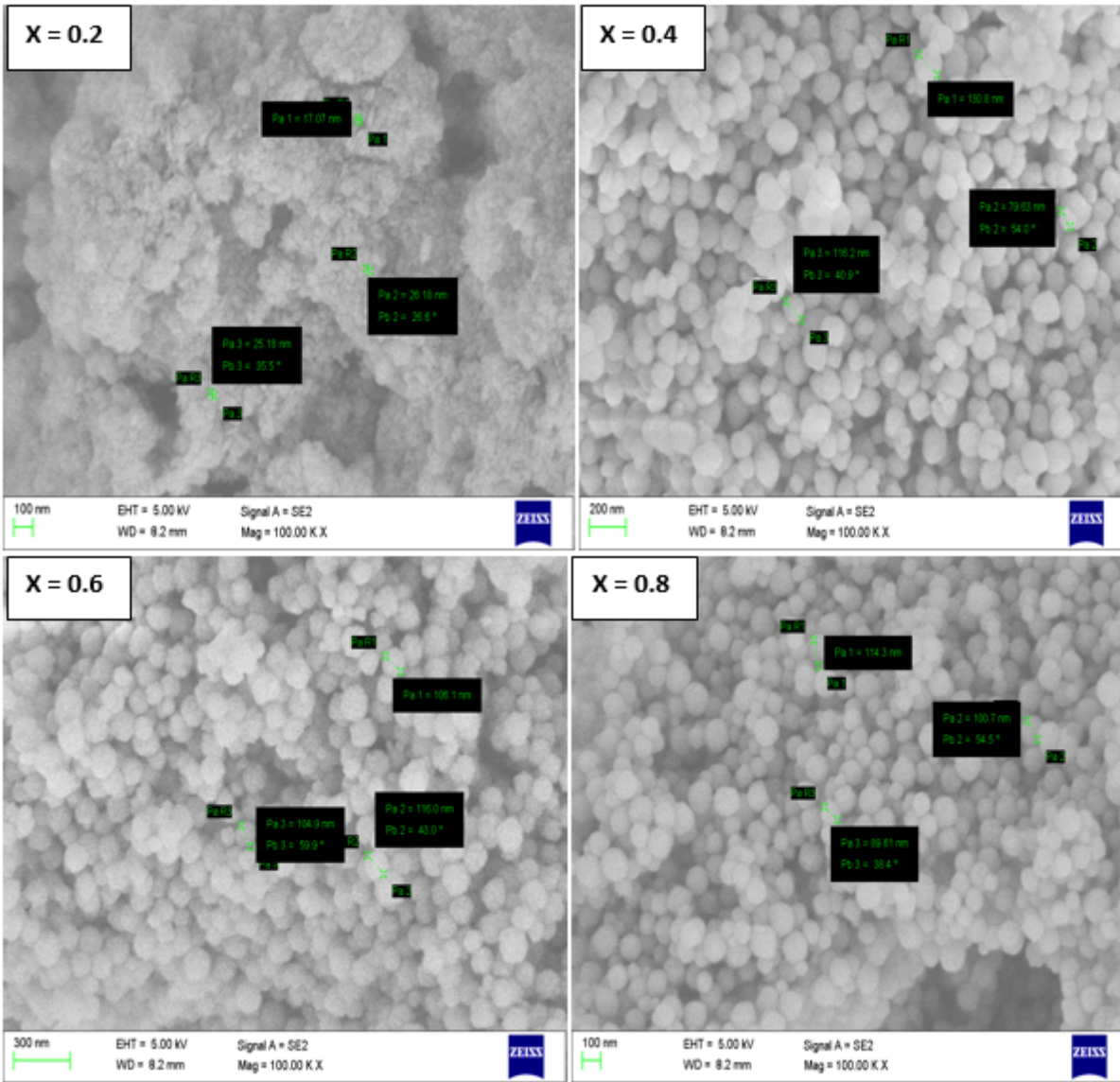


Figure 4

FESEM photos of SLFO nanoparticles

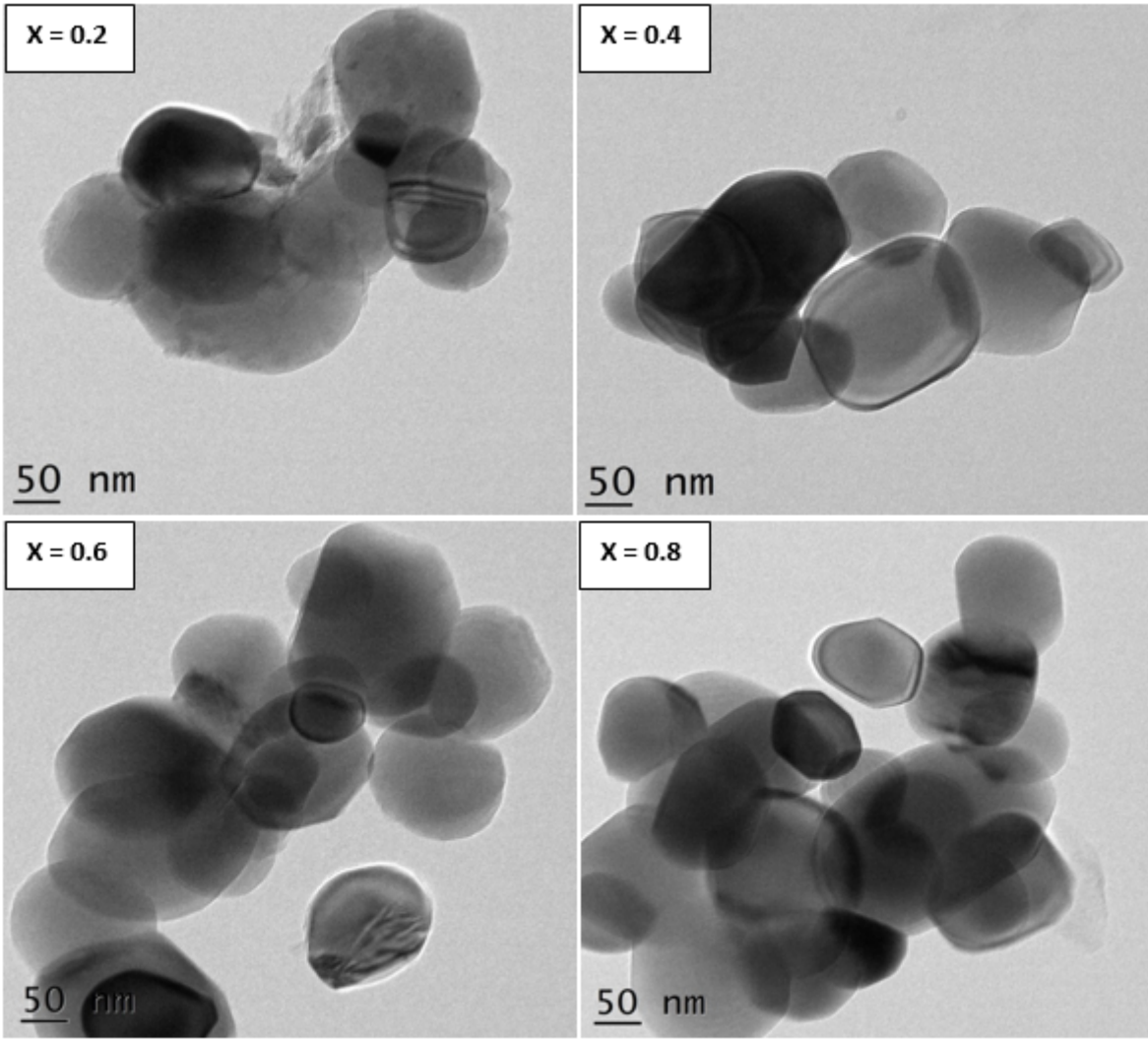


Figure 5

TEM photos of SLFO nanoparticles

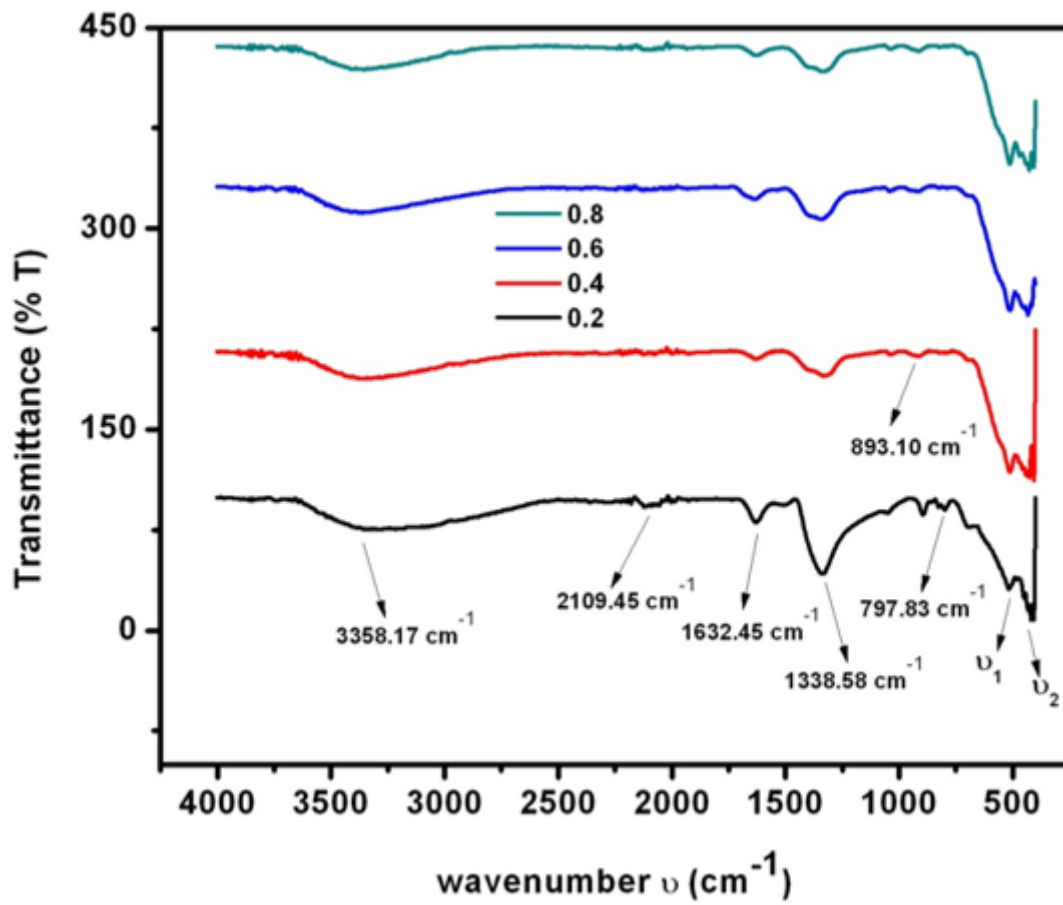


Figure 6

FTIR spectra of SLFO nanoparticles

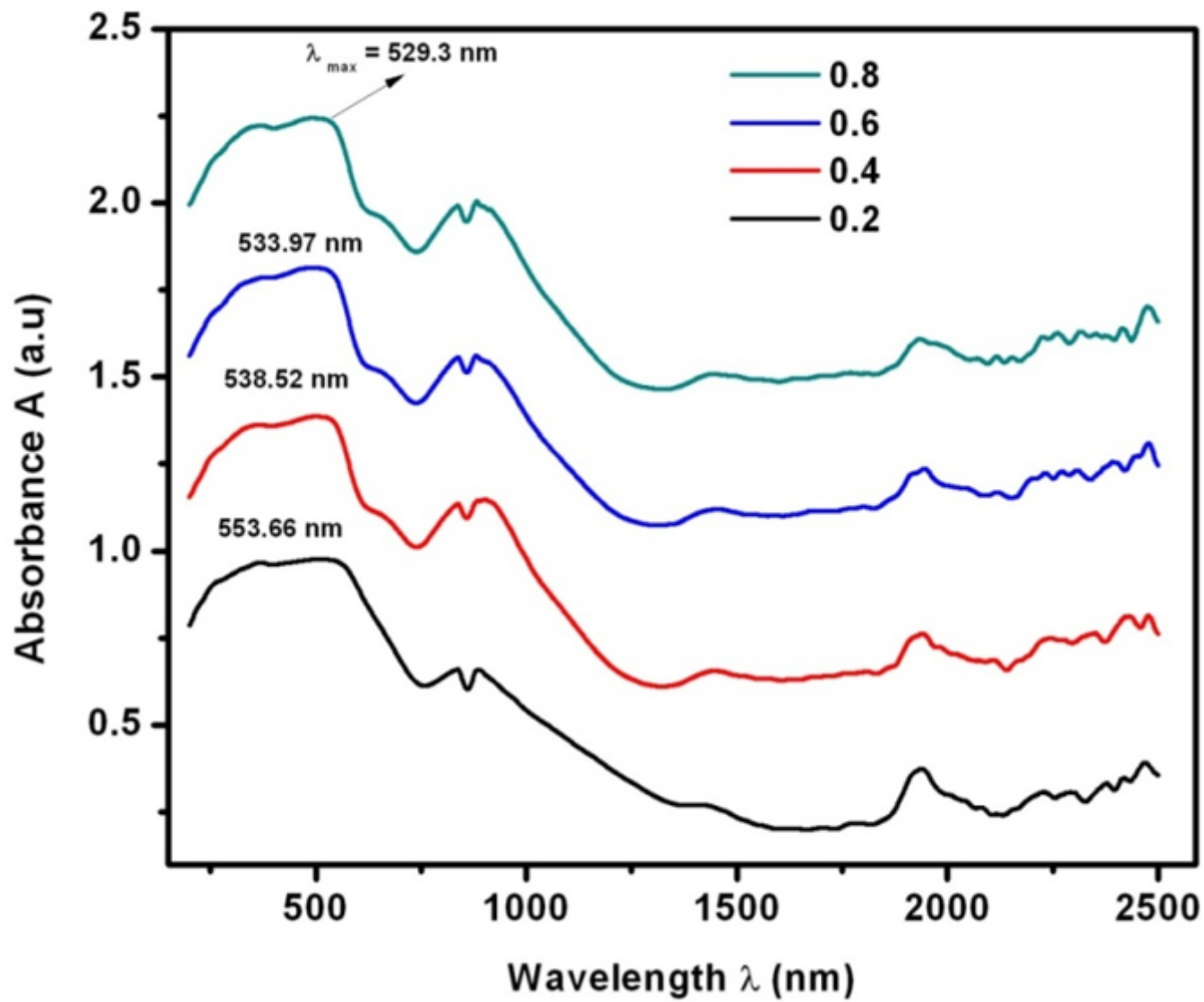


Figure 7

DRS spectra of SLFO nanoparticles

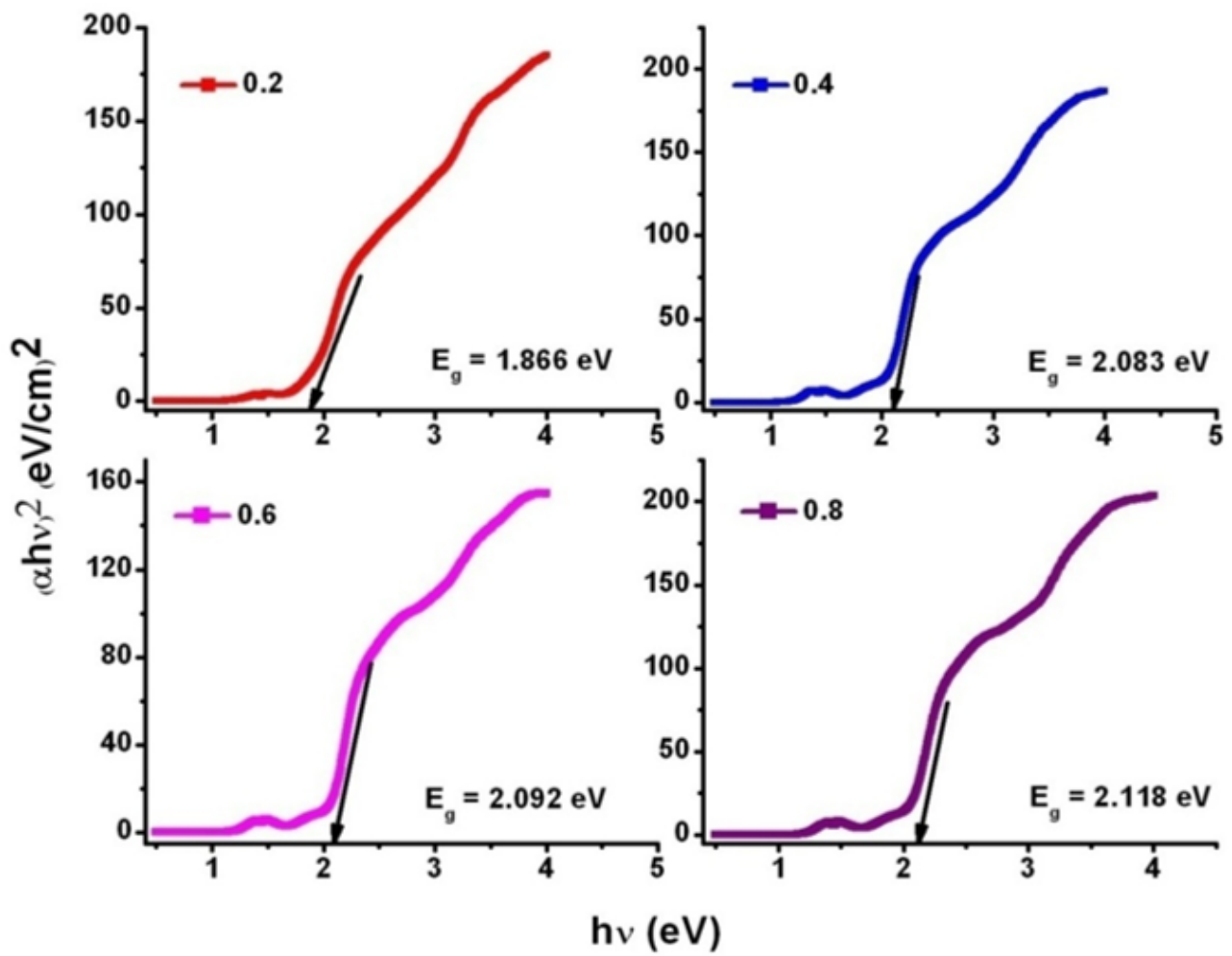


Figure 8

Optical bandgap determination of SLFO nanoparticles

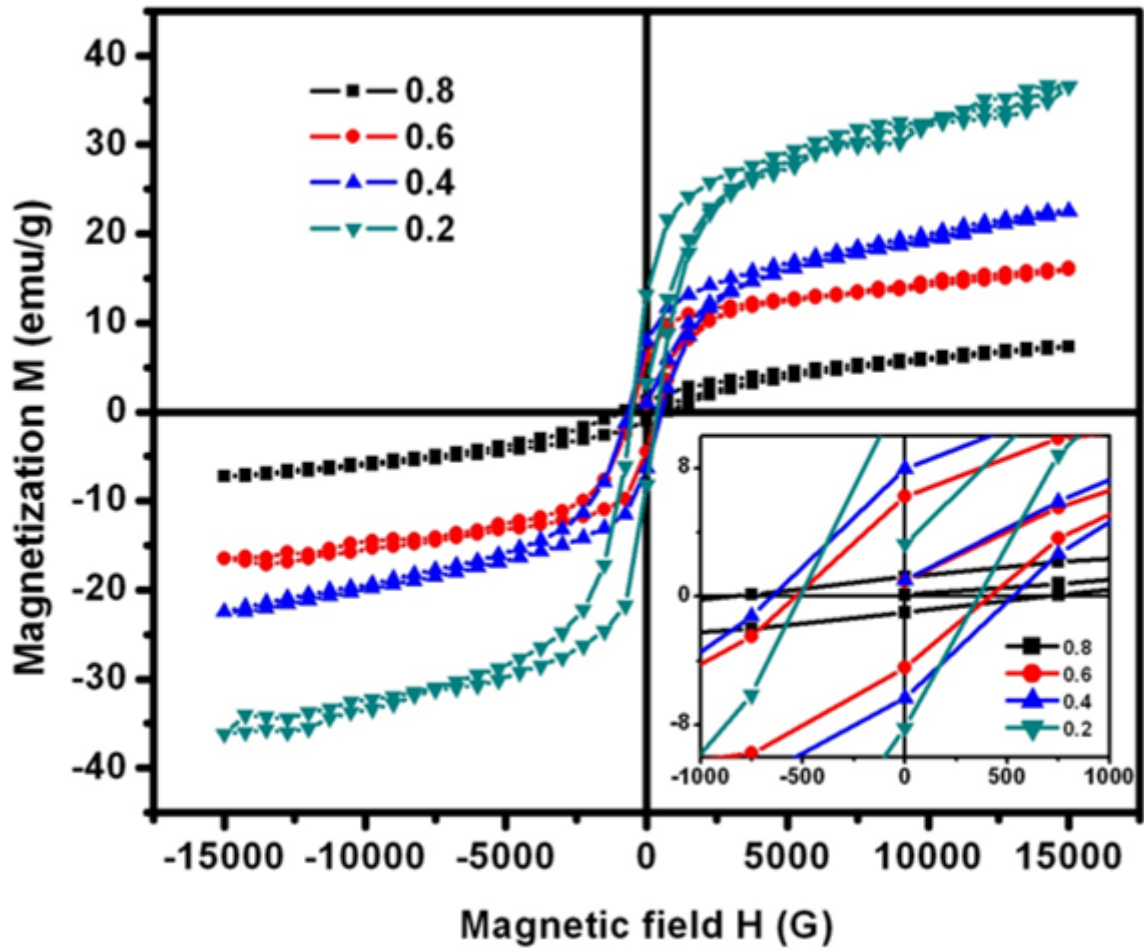


Figure 9

M-H loops of SLFO nanoparticles

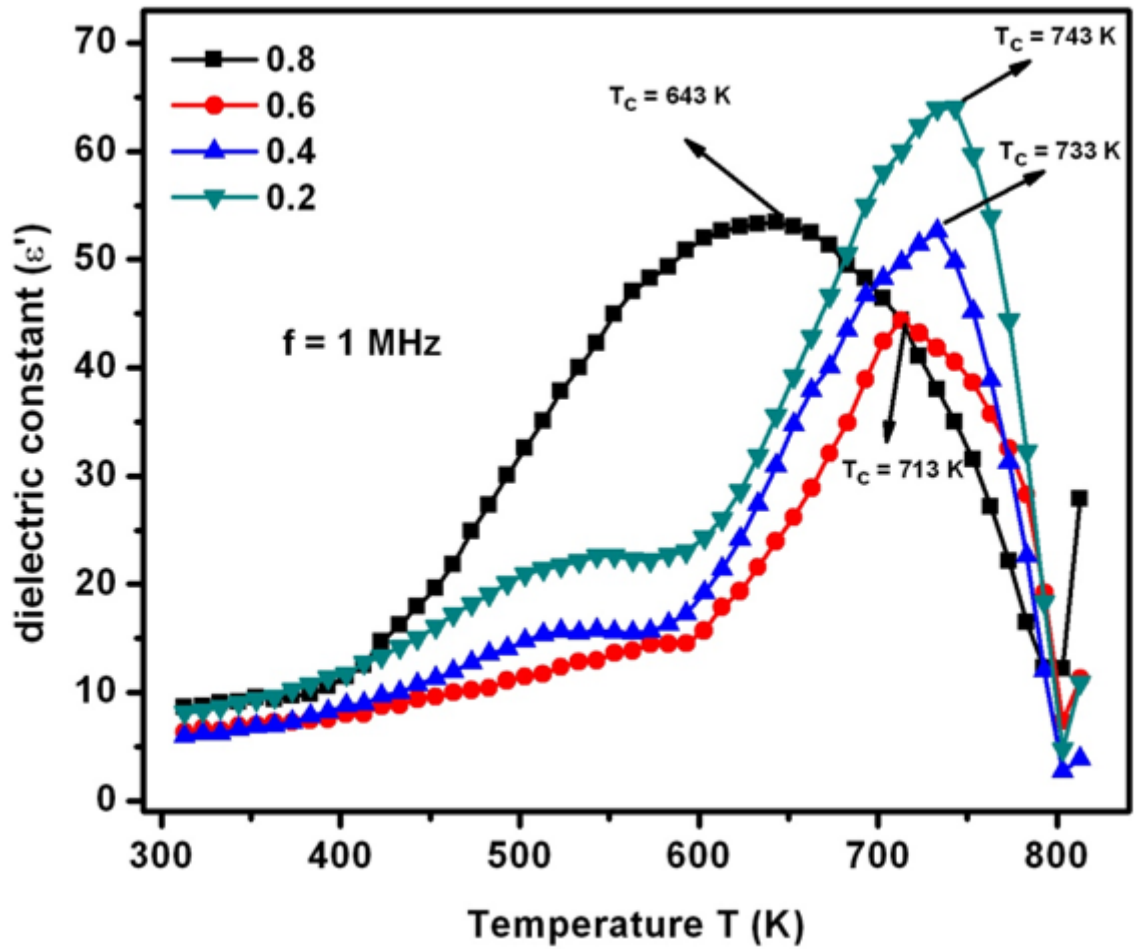


Figure 10

ϵ' -T plots of SLFO nanoparticles

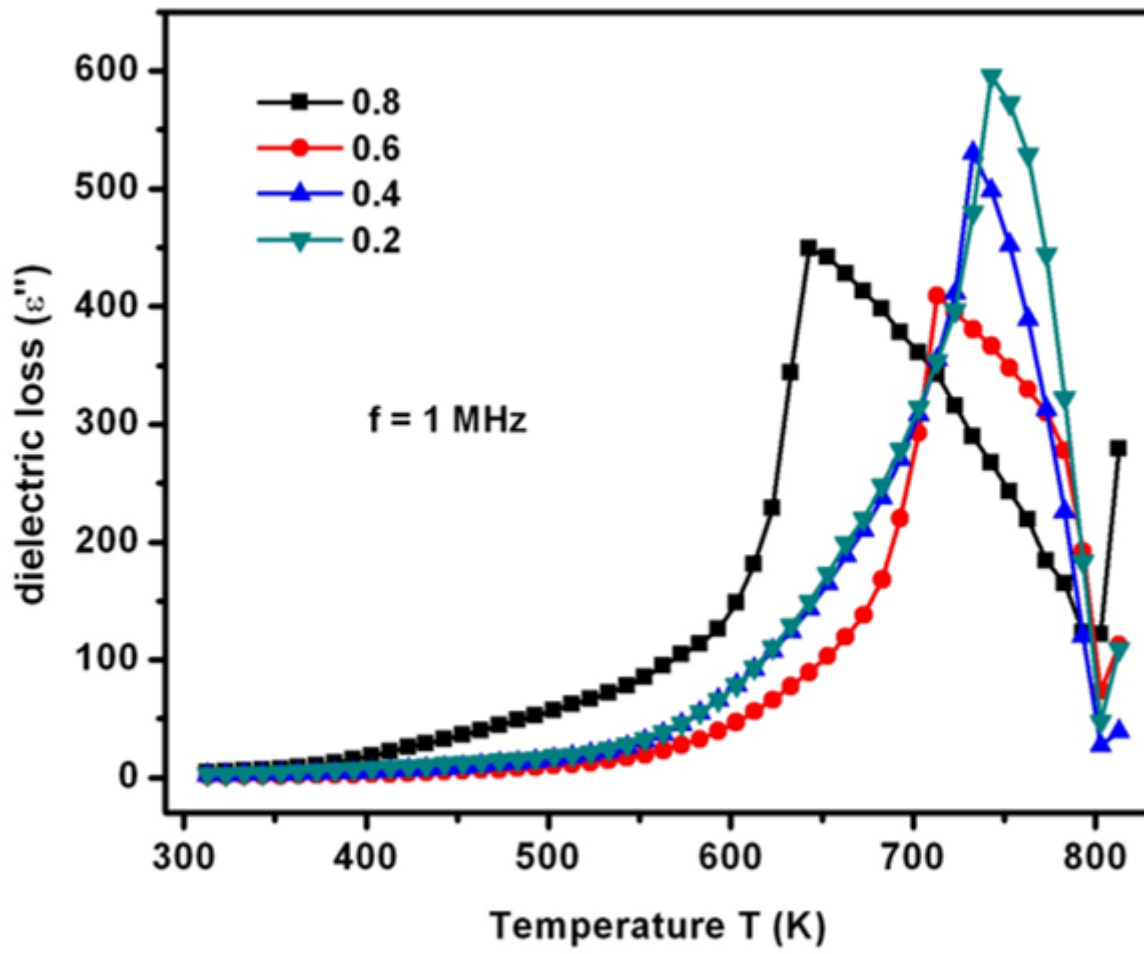


Figure 11

ϵ'' -T plots of SLFO nanoparticles

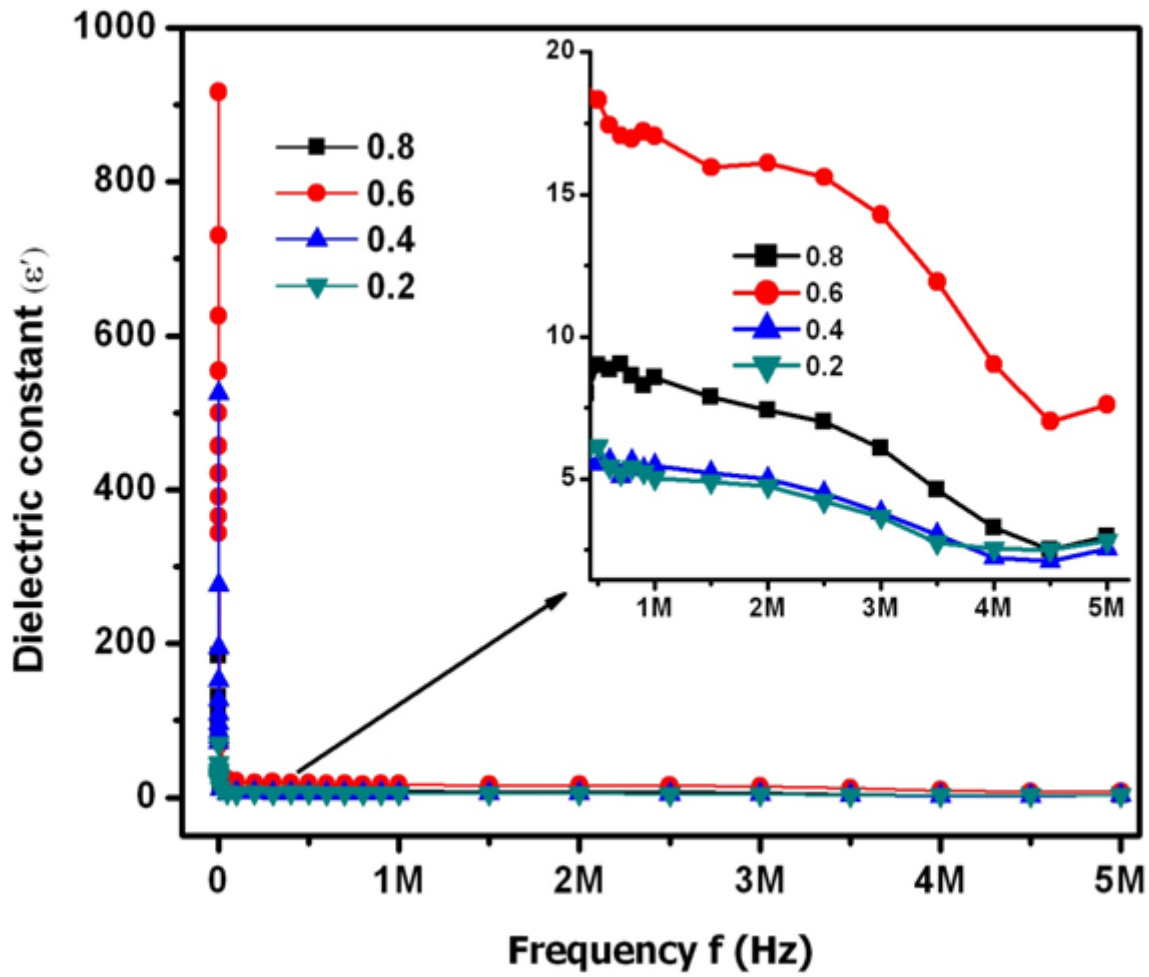


Figure 12

ϵ' - f plots of SLFO nanoparticles

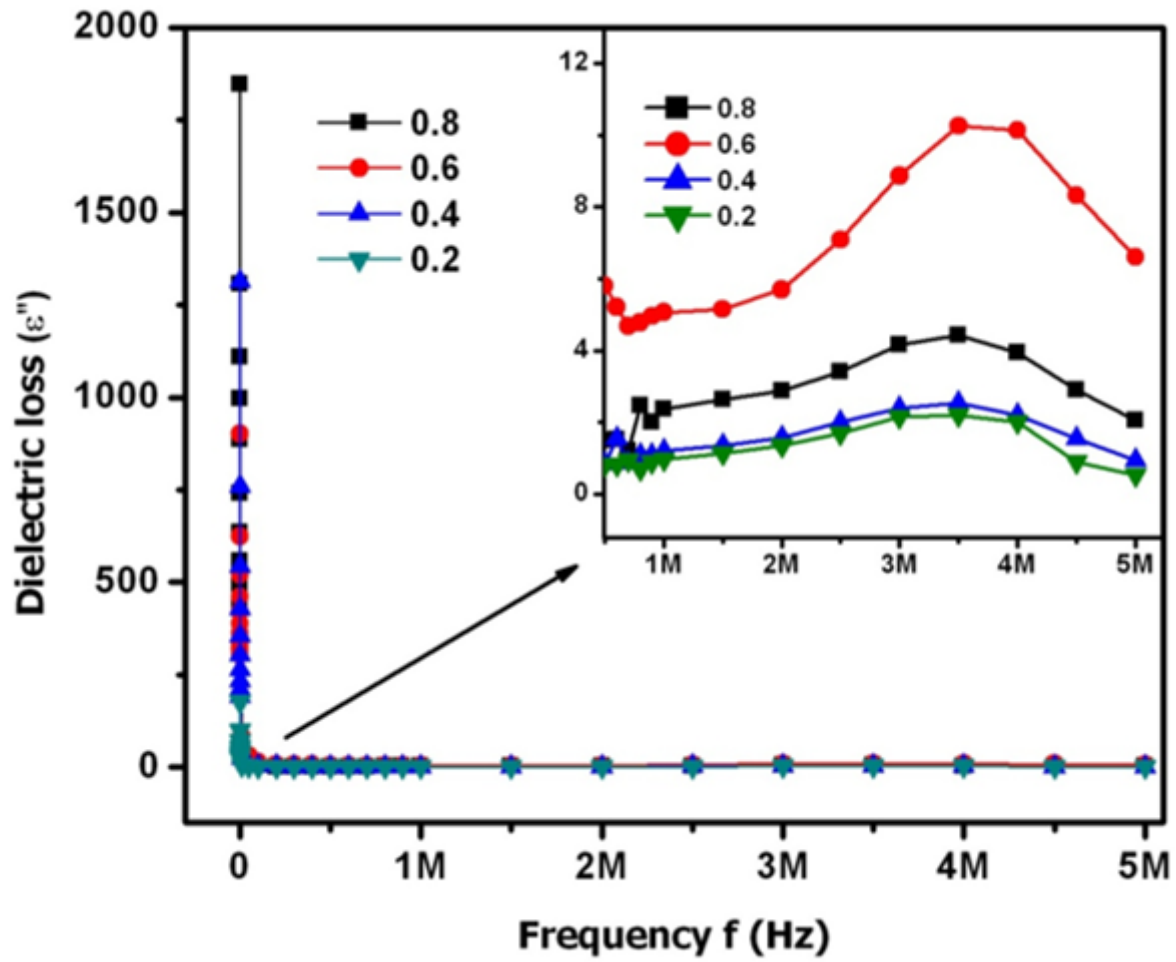


Figure 13

ϵ'' -f plots of SLFO nanoparticles

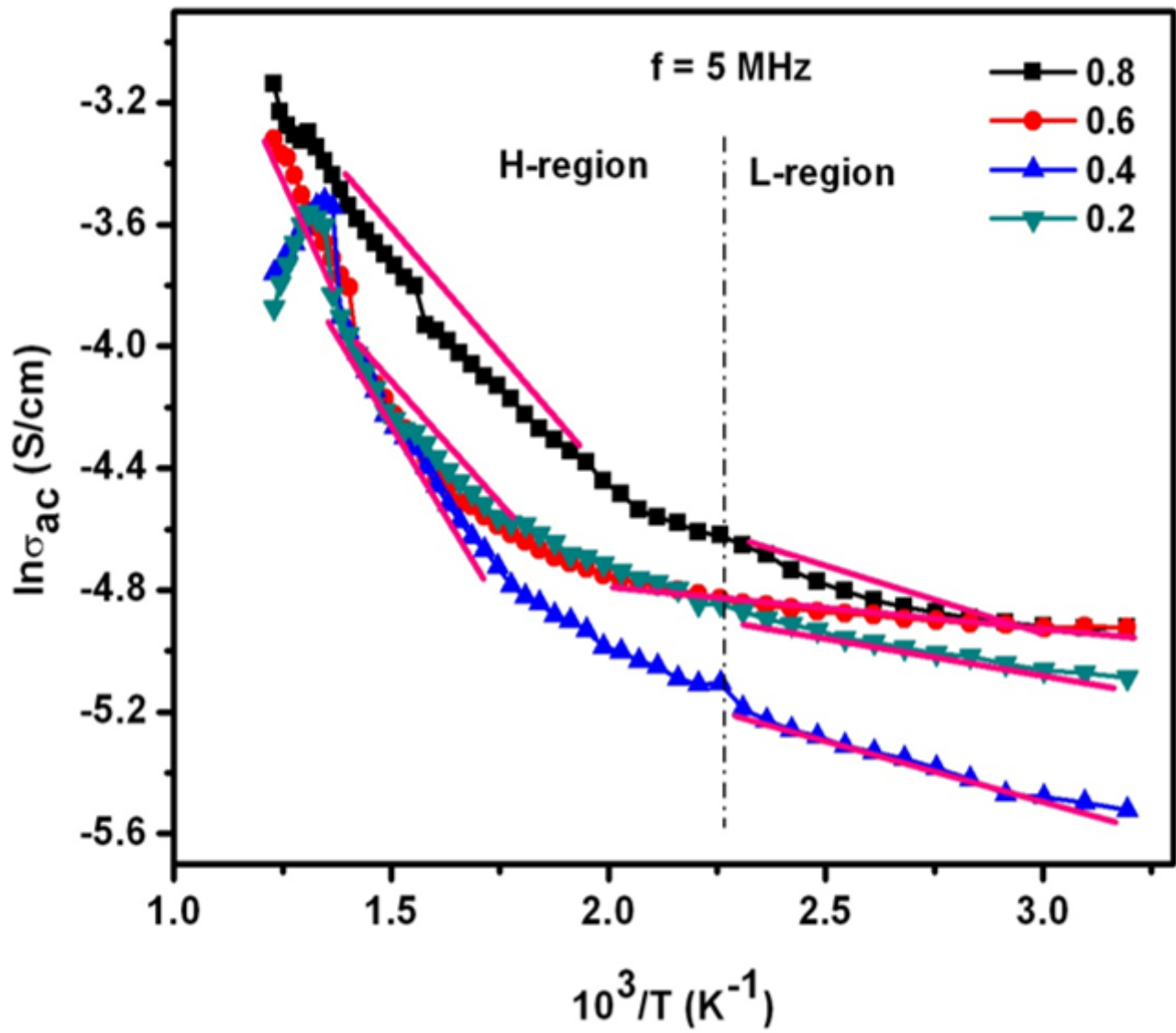


Figure 14

$\ln \sigma_{ac}$ versus $10^3/T$ plots of SLFO nanoparticles

Figure 15

$\log \sigma_{ac}$ versus $\log \omega$ plots of SLFO nanoparticles

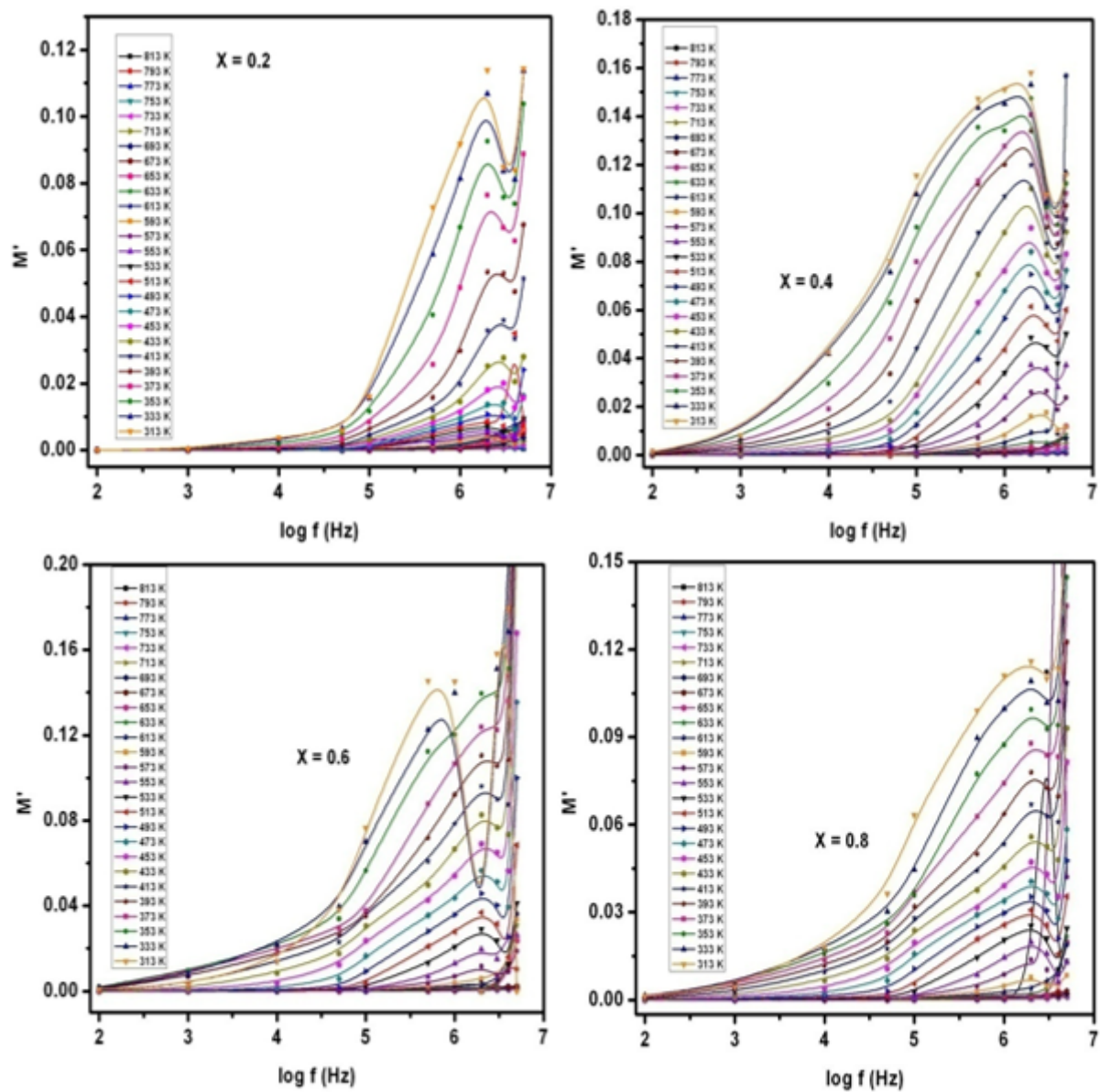


Figure 16

M' versus $\log f$ plots of SLFO nanoparticles

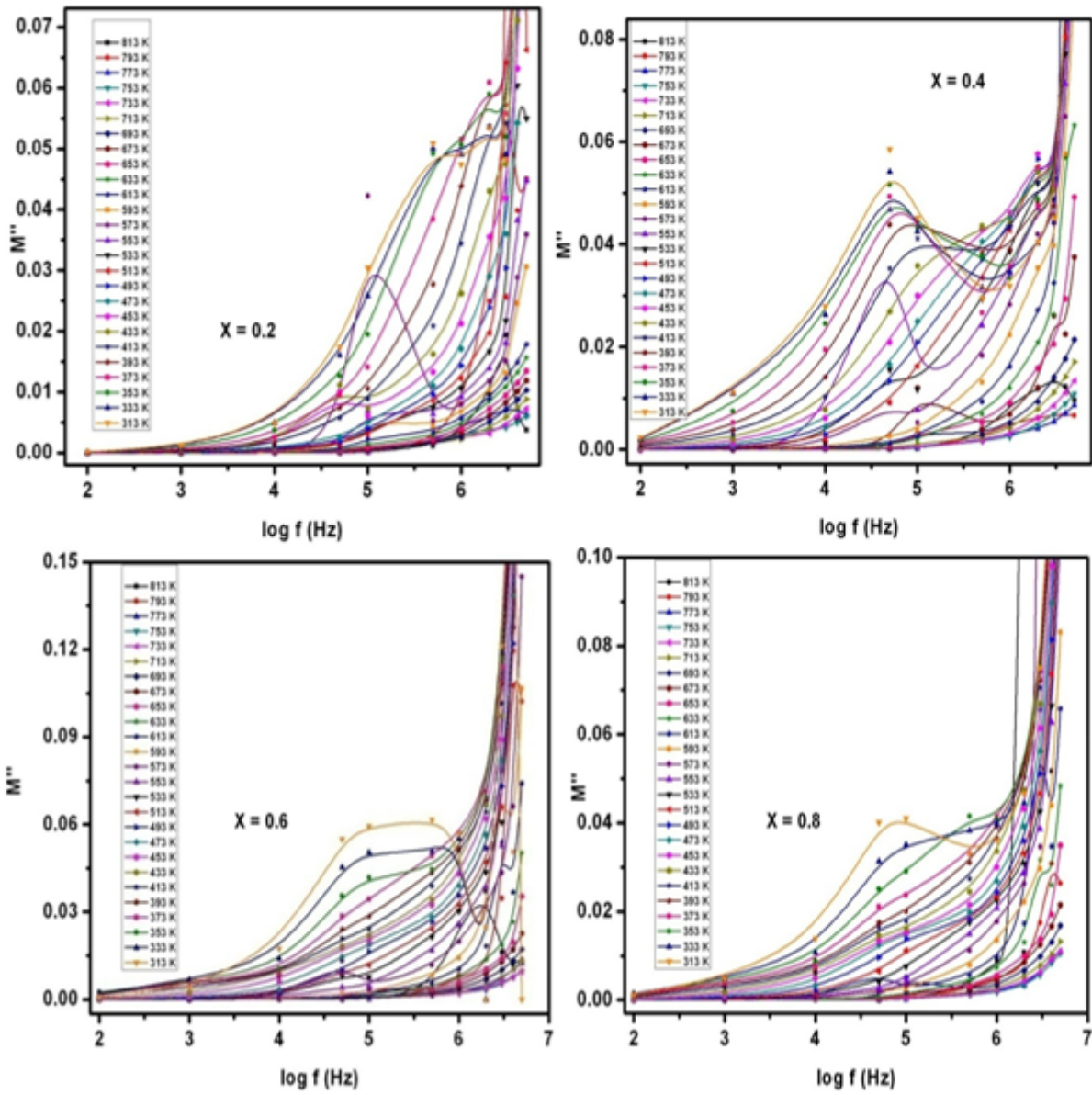


Figure 17

M'' versus $\log f$ plots of SLFO nanoparticles

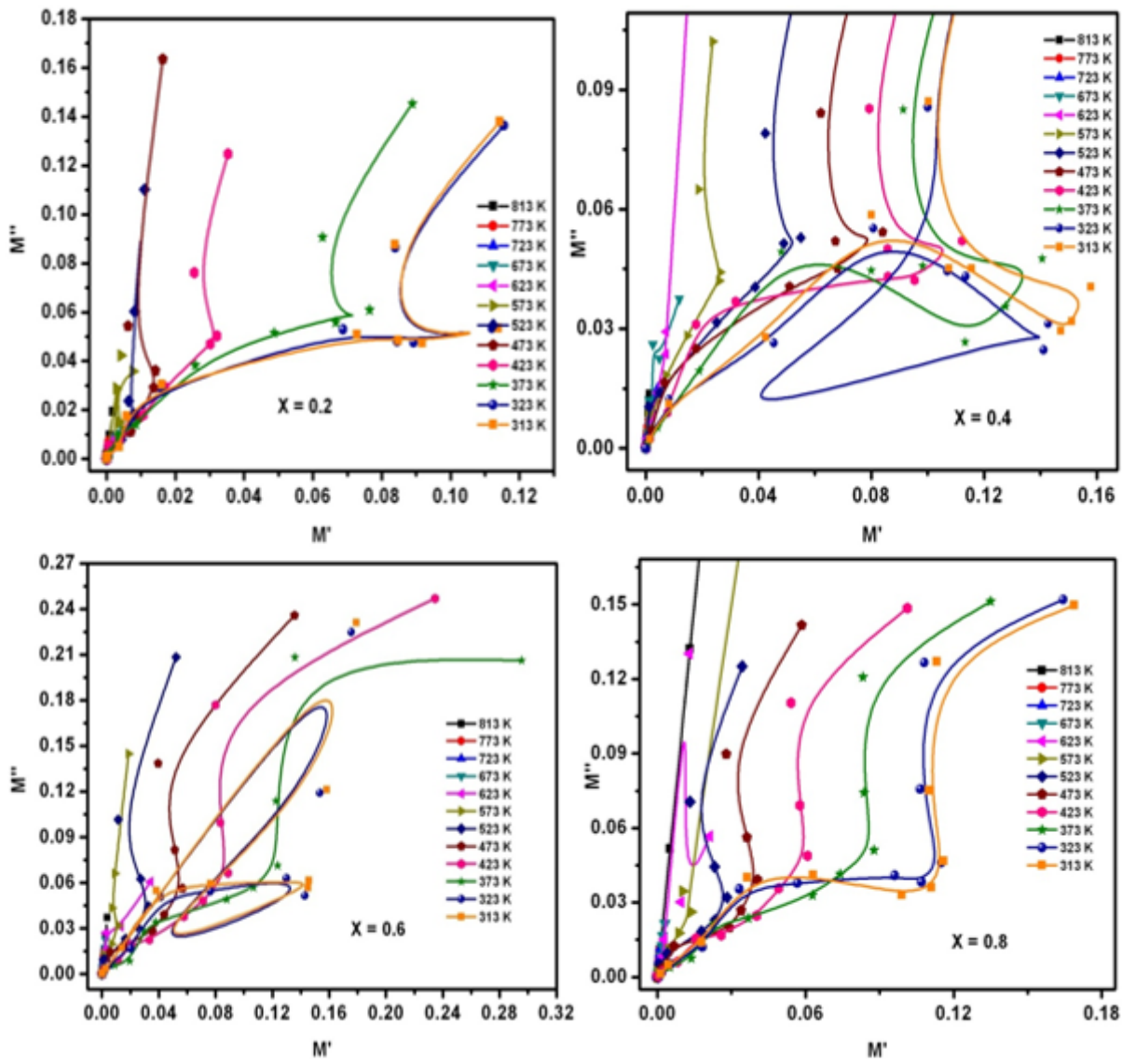


Figure 18

M' versus M'' versus $\log f$ plots of SLFO nanoparticles

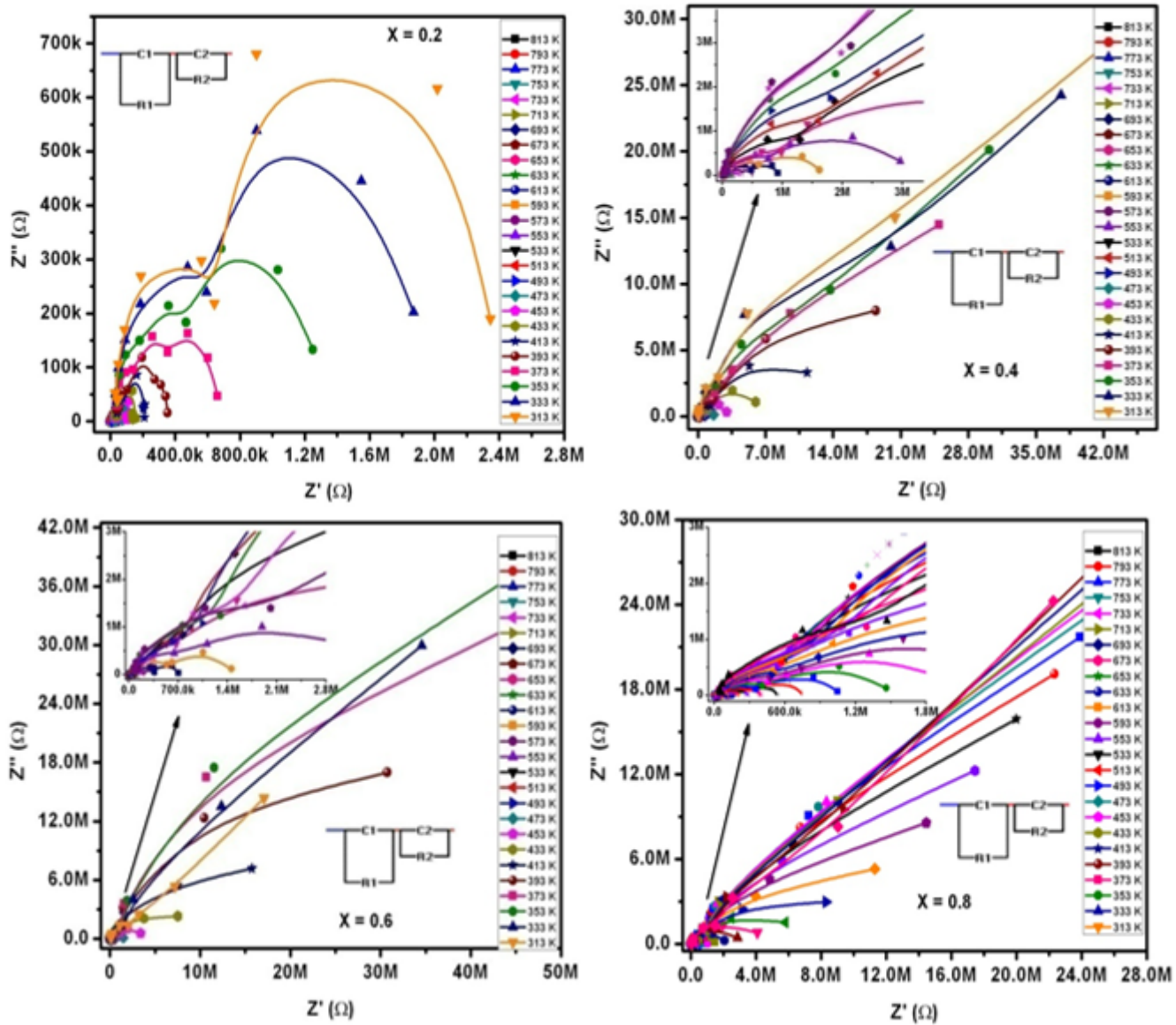


Figure 19

Z' versus Z'' versus $\log f$ plots of SLFO nanoparticles